



University College London

Department of Civil, Environmental & Geomatic Engineering

DISSERTATION:

**Evaluation of Uncertainties on Seismic Response of Eccentrically Braced Frames
with Self-Centring Links and Optimisation of the Self-Centring Link's
Performance**

*A dissertation submitted in partial fulfilment of the requirements for the Bachelor Degree
in Civil Engineering BEng*

by

Pui Man Wong

Chon Hou Lao

Supervisor: Dr. Fabio Freddi

Co-Supervisor: Ludovica Pieroni

Academic Year

2022-2023

Date of Submission

2023/04/07

Declaration and Personal Statement

The project has been carried out byPui Man Wong..... andChon Hou Lao.....

The authors have read and understood the College's policy regarding plagiarism and the submission of coursework. The authors confirm that, except for commonly understood ideas and concepts, or where specific reference is made to the work of other authors, the contents of this report are their own work. This dissertation is presented in 65 pages including bibliography and appendices. It contains approximately 10604 words, 32 figures and 7 tables.

Statement by: Pui Man Wong:

I estimate that my contributions to the parts of the project are as follows:

<i>Delete any of these that do not apply to your project</i>	%
literature review	50
theoretical development	50
computational work	50
data analysis	50
report writing and production	50
other (please specify)	
average	50

Signature:P.M.W.....

Date:2023/04/07.....

Declaration and Personal Statement

The project has been carried out byPui Man Wong..... andChon Hou Lao.....

The authors have read and understood the College's policy regarding plagiarism and the submission of coursework. The authors confirm that, except for commonly understood ideas and concepts, or where specific reference is made to the work of other authors, the contents of this report are their own work. This dissertation is presented in **65** pages including bibliography and appendices. It contains approximately **10604** words, **32** figures and **7** tables.

Statement by: Chon Hou Lao:

I estimate that my contributions to the parts of the project are as follows:

<i>Delete any of these that do not apply to your project</i>	%
literature review	50
theoretical development	50
computational work	50
data analysis	50
report writing and production	50
other (please specify)	
average	50

Signature:C.H.L.....

Date:2023/04/07..... .

Abstract

In the past several decades, innovative designs of low-damage systems were proposed to improve the repairability of seismic-resistant steel structures. One example was a self-centring eccentrically braced frame (SC-EBF) with the use of a damage-free self-centring link (SC-link). This SC-link composes of post-tensioned high-strength steel bars for self-centring effects and friction dampers to dissipate seismic energy. This paper studies the effect of uncertainties enclosed in the low-damage self-centring link (SC-link) on the seismic response of EBFs. Safety coefficients will further be developed to account for the uncertainties in future seismic designs. There are two main kinds of uncertainties: model uncertainties and record-to-record uncertainties. Predominant sources of model uncertainties include the friction coefficient of friction device, prestressed force in the bolts, and force in the post-tensioned bars (PT bars). Record-to-record uncertainties arise due to the discrepancies in seismic responses of structures under different ground motions. To evaluate the effect of the uncertainties, a case study is conducted on a four-storey EBF preliminary developed in compliance with Eurocode 8. 240 ground motions are selected for further analysis to account for record-to-record uncertainties. Monte Carlo method is adopted to select random design values of friction coefficients and forces in bolts and PT bars to account for model uncertainties. Then, an OpenSees model is built to carry out Modal Analysis and Non-linear Dynamic Analysis of the EBF under two sets of 240 ground motions to obtain seismic responses of the EBF. Engineering demand parameters (EDPs) and Ground-motion Intensity Measures (IM) are defined and used in the Probabilistic Seismic Demand Model (PDSM) and fragility test to evaluate seismic responses and the probability of structural failure under a given value of ground motion intensity. After the evolution of results, safety coefficients on the design of SC-links are developed.

Keywords: *Low-damage systems; Eccentrically braced frames; Damage-free self-centring links; Model uncertainties; Record-to-record uncertainties; Safety coefficients*

Table of Contents

Declaration and Personal Statement.....	i
Declaration and Personal Statement.....	ii
Abstract	iii
List of Figures	vi
List of Tables.....	viii
List of Symbols	ix
1 INTRODUCTION.....	1
1.1 Background and Motivation.....	1
1.2 Objective	3
1.3 Section Outline.....	3
2 LITERATURE REVIEW.....	3
2.1 Conventional Steel Frames.....	3
2.2 Low-damage Steel Eccentrically Braced Frames.....	5
2.3 Self-Centring Steel Eccentrically Braced Frames	6
2.4 Damage-free Self-centring Links for Eccentrically Braced Frames by Lettieri et al.	7
2.4.1 Working Principle	7
2.4.2 Existing Study on Uncertainty Evaluation.....	9
3 CASE-STUDY STRUCTURE AND FINITE ELEMENT MODELLING	10
3.1 Properties and Geometry	10
3.2 Finite Element Modelling.....	12
4 PERFORMANCE ASSESSMENT FRAMEWORK.....	16
4.1 Evaluation of Uncertainties.....	16
4.1.1 Classification of Uncertainty.....	16
4.1.2 Implementation of Monte Carlo Simulation	17
4.1.3 Computation of the Hysteretic Behaviour of SC-link	20
4.1.4 Cloud Analysis	22
4.2 Optimisation of SC-link Model.....	28
5 RESULTS AND DISCUSSION	30
5.1 Impact of Uncertainties on SC-EBF.....	30
5.1.1 Hysteretic Behaviour.....	30
5.1.2 Engineering Demand Parameters	33
5.1.3 Fragility Curves of Residual Interstorey Drift Ratio.....	42
5.2 Optimisation of SC-Link.....	44
6 CONCLUSION	49

7	FUTURE WORK	51
8	Reference.....	52

List of Figures

Figure 1 – Seismic Performance Design Objective Matrix as defined by SEAOC Vision 2000 Committees [4].....	2
Figure 2 – Types of conventional steel frames and their respective dissipative zones (heavy black lines and grey) [8]	4
Figure 3 – Hysteretic behaviour of conventional steel frames, adopted from Zhong et al. [15]...	6
Figure 4 – Hysteretic behaviour of self-centring systems, adopted from Zhong et al. [15].....	6
Figure 5 – Demonstration of the components in SC-link extracted from Lettieri et al. [24]	8
Figure 6 – Demonstration of a oscillating SC-EBF extracted from Lettieri et al. [24]	9
Figure 7 – Hysteretic longitudinal shear vs displacement graph showing point 1- 5.....	9
Figure 8 – 5x4 case-study frame adopted from Lettieri et al. [24]: (a) Plan view; (b) Elevation view	11
Figure 9 – Available options to model plasticity in Opensees extracted from Reinhorn et al. [27]	13
Figure 10 – (a) Positions of nodes and (b) Positions of elements of the simplified SC-EBF	13
Figure 11 – Demonstration of the SC-EBF showing (a) Leaning columns, and (b) SC-link and Panel zone	16
Figure 12 – General hysteretic loop showing parameters of “ <i>SelfCentring</i> ” materials, adopted from Jeff Erochko et al. [28]	16
Figure 13 – A set of 240 ground motions adopted from Jayaram et al. [31].....	19
Figure 14 – Distributions of μ , F_p, PT and F_p, FD of SC-links on each storey and sample selection by Monte Carlo Simulation: a) sample selection of μ ; b) sample selection of F_p, PT ; c) sample selection of F_p, FD	19
Figure 15 – Deformed shape of SC-EBF adopted from Lettieri et al. [24].....	21
Figure 16 – Free-body diagram of the forces acting on SC-EBF adopted from Lettieri et al. [24]	22
Figure 17 – Transverse shear force (V) vs. link rotation (θ) graph with $V1, V2, V3, V4$ defined	22
Figure 18 – a) Accelerograms of the selected 30 ground motions; b) Accelerograms scaled at the ULS intensity	29
Figure 19 – Comparison of hysteretic loops at FPTFFD = 0.500.50 between a) cases without uncertainties and.....	31
Figure 20 – Transverse shear force V vs. link rotation (θ) graphs of storey 4 of SC-EBF as FPTFFD varies from 0.100.90 to 0.900.10	32
Figure 21 – Theoretical relationship between peak interstorey storey drift ratio ($IDRpeak$) and spectral acceleration ($SaT1$)	33
Figure 22 – Plots of peak interstorey drift ratios ($IDRpeak$) at storey 4 of SC-EBF under accelerations as FPTFFD varies from 0.100.90 to 0.900.10	34
Figure 23 – Linear regression of peak interstorey drift ratios ($IDRpeak$) at storey 4 of SC-EBF under accelerations as FPTFFD varies from 0.100.90 to 0.900.10	35
Figure 24 – Plots of peak link rotations (\thetapeak) at storey 4 of SC-EBF under accelerations as FPTFFD varies from 0.100.90 to 0.900.10	37
Figure 25 – Linear regression of peak link rotations (\thetapeak) at storey 4 of SC-EBF under accelerations as FPTFFD varies from 0.100.90 to 0.900.10	38
Figure 26 – Logarithmic plots of residual drift ratios at storey 4 of SC-EBF under accelerations as FPTFFD varies from 0.100.90 to 0.900.10.....	40

Figure 27 – Plots of residual drift ratios (IDR_{res}) at storey 4 of SC-EBF under accelerations as FPTFFD varies from 0.100.90 to 0.900.10	41
Figure 28 – Fragility curves for residual interstorey drift ratio IDR_{res} with a threshold of DS1 = $1 \times 10 - 10\%$ at storey 4 as FPTFFD varies from 0.100.90 to 0.900.10	43
Figure 29 – General trends of residual interstorey drift ratio (IDR_{res}) as FPTFFD varies from 0.100.90 to 0.900.10	45
Figure 30 – General trends of peak interstorey drift ratio (IDR_{peak}) as FPTFFD varies from 0.100.90 to 0.900.10	45
Figure 31 – General trends of peak link rotation θ_{peak} as FPTFFD varies from 0.100.90 to 0.900.10	45
Figure 32 – Hysteretic behaviour in terms of transverse shear force V vs. link rotation (θ) as FPTFFD varies from 0.500.50 to 0.600.40	48

List of Tables

Table 1 – Design Summary of the simplified EBF adopted from Lettieri et al. [24].....	11
Table 2 – Design Summary of the SC-links adopted from Lettieri et al. [24]	11
Table 3 – Section Properties of the SC-links adopted from Lettieri et al. [24]	12
Table 4 – Comparison of plasticity models.....	13
Table 5 – Coefficient of variation (COV) of μ , F_p , PT and F_p , FD	17
Table 6 – 9 sets of $FPTFFD$ ratios considered in the cloud analysis.....	23
Table 7 – Threshold capacities of $IDRpeak$, $\theta peak$ and $IDRres$	26

List of Symbols

Abbreviation	Definition	Unit
μ	Dynamic friction coefficient of the friction device, which is one of the sources of model uncertainties	[-]
θ_{peak}	Peak link rotation	radian
Δ_{max}	Maximum frame sway displacement	[-]
Δ_{res}	Residual frame sway displacement	[-]
COV	Coefficient of variation	[-]
C	Capacity	[-]
D	Demand	[-]
EBF	Eccentrically braced frame	[-]
EDP	Engineering demand parameter	[-]
e	Length of self-centring link	m
$F_{p,FD}$	Preloading force in each of the bolts in the friction device, which is one of the sources of model uncertainties	kN
$F_{p,PT}$	Post-tensioning force in each of the PT-bars, which is one of the sources of model uncertainties	kN
F_{FD}	Total friction force in the friction device	kN
F_{PT}	Total post-tensioning force in the PT-bars	kN
$\frac{F_{PT}}{F_{FD}}$	Ratio of the total post-tensioning force in the PT-bars to the total friction force in the friction device	[-]
F	Total shear force	kN
F_l	Longitudinal shear force	kN
FD	Friction device	
H	Storey height	m
h_d	Section height of the link	m
IDR_{peak}	Peak interstorey drift ratios	%
IDR_{res}	Residual interstorey drift ratio	%
IM	Intensity measure	[-]
L	Span of the frame	m
n_s	Number of friction interfaces	[-]
n_b	Number of bolts	[-]
PT	Post-tensioned	[-]

$S_a(T_1)$	First-mode spectral acceleration of the fundamental period	g
SC	Self-centring	[\cdot]
T	Period	s
t_f	Flange thickness	m
V	Transverse shear force	kN

1 INTRODUCTION

1.1 Background and Motivation

Earthquake is one of the natural disasters that lead to millions of casualties and severe impacts on society every year. This can be visualised in an earthquake with a Richter value of 8.0 hitting Sichuan, China in 2008. This earthquake has caused approximately 70000 deaths, more than 370000 injuries and an economic loss of 127 billion US dollars [1]. To reduce the risk associated with earthquakes, the conventional seismic design philosophy suggested by current codes focuses on the prevention of the collapse of buildings by dissipating seismic energy. Conventional structures are designed to have “weak” elements which undergo large plastic deformation during seismic events. These elements are lower in stiffness and strength compared to other structural components, allowing themselves to be yielded. Thus, the damage due to earthquakes will effectively be limited to the predetermined locations, preventing the collapse of buildings [2,3].

Despite that the invention of EBFs highly limits residual drifts and improves energy dissipation, repairing EBFs after an earthquake can be difficult and expensive as the entire link and beam may need repair. The time-consuming repair process of EBFs significantly affects the serviceability of buildings, resulting in disruption of society especially when structures like hospitals and fire stations become nonoccupational after earthquakes. Recognising the drawbacks of the conventional seismic lateral force-resisting systems, alternative designs of seismic-resilient structures must be proposed. To control the amount of damage experienced by buildings, SEAOC Vision 2000 Committee (1995) introduced a performance-based design approach [4]. A Seismic Performance Design Matrix following SEAOC Vision 2000 PBSE Guidelines was prepared by Pampanin [4] and shown in Figure 1. The blue line on the matrix suggests the recommended level of repairability of buildings under different levels of frequency in the occurrence of earthquakes. It can be inferred that buildings located in areas suffering from earthquakes every 43-72 years should be fully operational after earthquakes, while buildings in places with rare occurrences of earthquakes should be operational.

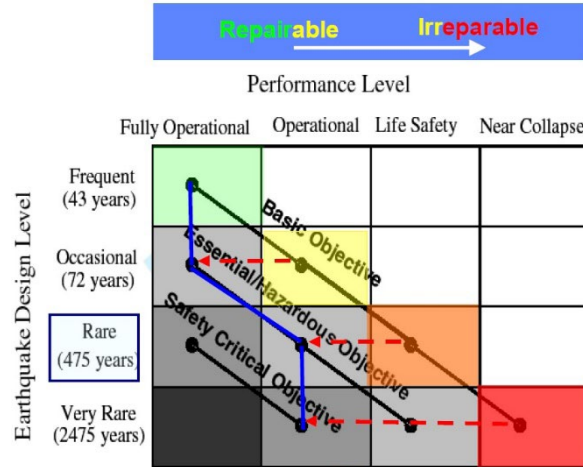


Figure 1—Seismic Performance Design Objective Matrix as defined by SEAOC Vision 2000 Committees
[4]

To ensure the buildings can be operational as soon as possible, the repair process should be simplified to reduce downtime. Hence, different seismic-resilient systems which promise low damage, low repair costs and low downtime were proposed and studied in the past few decades. However, since these systems are still in their initial design stages, there has been a lack of comprehensive design criteria and guidelines to regulate them. This can result in overestimation of their seismic performance such as their structural stability and resilience, which can be hazardous since the buildings may deform or even collapse before reaching their designed capacity, resulting in catastrophic accidents. Therefore, it is crucial to assess the potential uncertainties and their impact on these systems before introducing them to the market to ensure their seismic resistance. This underpins the fundamental objective of this study – to evaluate the effect of enclosed uncertainties in one of the recently proposed seismic resilient system and to propose ways to improve their seismic resilience.

1.2 Objective

This paper aims at evaluating and providing insights on an innovative seismic resilient system proposed by Lettieri et al. [5] — an eccentrically braced steel frame (EBF) equipped with self-centring links (SC-links). Specifically, this study focuses (i) exploring the associated uncertainties in the SC-link model and their impact on the frame's seismic resistance and (ii) optimising the seismic performance of the SC-EBF by improving the self-centring behaviour and energy dissipation ability of the self-centring link model.

1.3 Section Outline

Section 2 presents the literature review which includes the development of low-damage device, the working principle of SC-link discussed in this paper and the general approach of uncertainty evaluation.

Section 3 presents the case-study structure and the modelling methodology of the finite element model in OpenSees.

Section 4 presents the performance assessment framework of the SC-link, including the classification of main source of uncertainties and the methodology of analyses.

Section 5 discusses the results obtained from analyses and identify impact of uncertainties on the SC-EBF's performance. The optimisation of SC-link model is also described.

Section 6 and 7 summarise the whole paper and presents future work for improvements.

2 LITERATURE REVIEW

2.1 Conventional Steel Frames

Conventional MRFs are characterised by having weaker beams and a rigid beam-column jointing system. MRFs have high ductility but low stiffness. Since the maximum moment is usually developed at the ends of structural elements, plastic hinges are formed at the beam ends to dissipate energy. However, with a significant number of laboratory tests conducted by Gledhill et al. [3], it is concluded that MRFs become unserviceable and disruptive to be repaired after experiencing seismic events. Despite the introduction of several designs such as “PRESSS” frames and sliding hinge joints which prevent the local damage on beam ends, global residual

drifts are still seen due to beam elongation effect and loss of elastic strength and stiffness once subjected to seismic events [3,4,6].

For CBFs, energy dissipation is concentrated at high-strength concentric braces by yielding in tension and buckling in compression. CBFs are designed to possess significantly higher stiffness than other systems, resulting in lower residual deformations. A noticeable issue of CBFs is their different strengths in compression and tension which make steel bracings unable to dissipate as much energy in compression as in tension, hence limiting energy dissipating capacity [7]. This shortcoming was overcome by incorporating buckling restrained braces (BRB) and friction braces in the system, in which similar behaviour in both compression and tension was observed [8]. Nevertheless, due to the difficulties in evaluating the amount of energy absorbed in the braces and the cost of replacement, further studies on their applications are required.

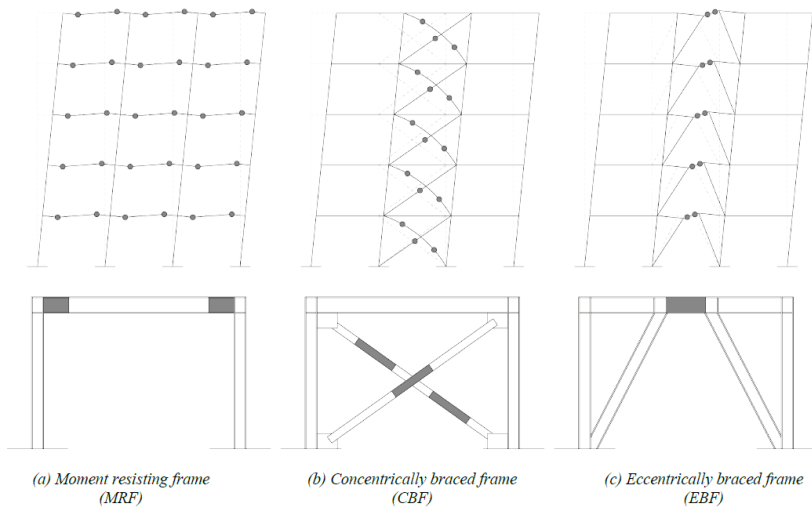


Figure 2 – Types of conventional steel frames and their respective dissipative zones (heavy black lines and grey) [9]

To combine the individual advantages of MRFs (large ductility to provide excellent energy dissipation capacity) and CBFs (high stiffness to limit residual drift), eccentrically braced frames (EBFs) which is a hybrid between MRFs and CBFs were proposed. One distinguishing feature of EBFs is that one or both ends of the diagonal braces are not connected at the endpoints of other framing members. The induced brace forces are transferred to other structural elements through the links [7][10]. Links are designed to be the weakest members in the structure and energy

dissipators. Links deform in different ways depending on their lengths. Short links dissipate energy predominantly by shear while long links dissipate energy by bending [2].

2.2 Low-damage Steel Eccentrically Braced Frames

Gregory et al. [8] introduced several approaches to improve the repairability of steel structures. Among others, the inclusion of replaceable links in steel EBF was investigated. Stratan et al. [11] pioneered the first replaceable link to be included in EBF through bolted connections between the link and beams' ends. By modelling links with low-yield steel, energy dissipation is concentrated at links which reduce global damages. Extensive research was done by Dubina et al. [12] to examine the behaviour of EBF with replaceable links under cyclic loads. It was validated that EBFs with replaceable links demonstrate larger interstorey displacements and demand for inelastic deformation than conventional links, meaning larger residual drifts may occur. One drawback regarding this design is that although concentrating damage at replaceable links eases the repair of the structure after an earthquake, EBFs should be realigned to their original configurations before replacements of links can be done, making the repair of structures difficult. To prevent unsuccessful replacement due to misalignment of beam ends, several other EBF systems have been presented. Among others, Dubina et al. [13] proposed incorporating replaceable links in dual high-strength steel eccentrically braced frames. The dual system is a combination of eccentrically braced frames with replaceable links (rigid subsystem) and moment-resisting frames (flexible subsystem). Moment-resisting frames provide extra recentring capacity to the dual system which results in reduced residual displacements and misalignment of beams. A similar study was done by Mansour et al. [14] in which the feasibility of using welded connections in web-connected links was experimentally investigated. Using welded instead of bolted connections allows replacements to be done by flame-cutting of links from the adjacent beams. Thus, no realignment of the frame is necessary. However, in both EBFs proposed by Dubina et al. and Mansour et al. [13,14], hydraulic jacks with 500 kN capacity must be utilised to push the beams apart for the replacement of links. The need for extra machinery in the repair process induces machinery costs so the effectiveness of these EBFs in reducing repair costs should be further addressed [12]. Bozkurt et al. [15] presented another replaceable link with direct brace attachment. This link eliminated the need for hydraulic jacks during the replacement of links while enabling a reduction in link section depth, hence allowing for lower repair costs.

Although a considerable number of studies were done to confirm the feasibility of the above-presented EBFs to low repair costs by limiting repair at links, they were investigated under the premise of minimal residual deformation and the effect of residual drifts in the repair process was never taken into consideration. Unfortunately, in the reality, there are typically large residual

deformations in EBFs due to their hysteretic behaviour. Figure 3 illustrates that after lateral loads are removed, residual drifts are formed due to the accumulation of energy dissipation at the plastic links.

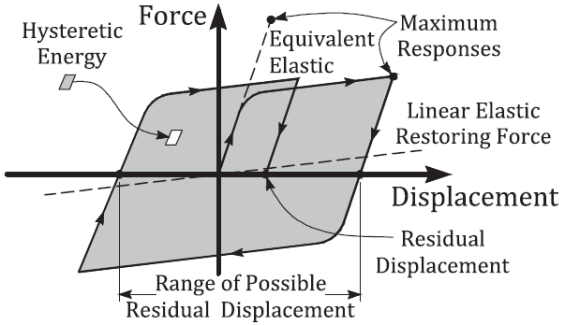


Figure 3 – Hysteretic behaviour of conventional steel frames, adopted from Zhong et al. [16]

2.3 Self-Centring Steel Eccentrically Braced Frames

Self-Centring Eccentrically Braced Frames (SC-EBFs) are defined as seismic-resilient systems which are capable of returning to their original configurations after earthquakes [17]. SC systems are characterised by flag-shape hysteretic energy dissipation loops as illustrated in Figure 4. Although SC systems have lower energy dissipation capacity than conventional systems, they exhibit zero residual drifts after lateral loads are removed.

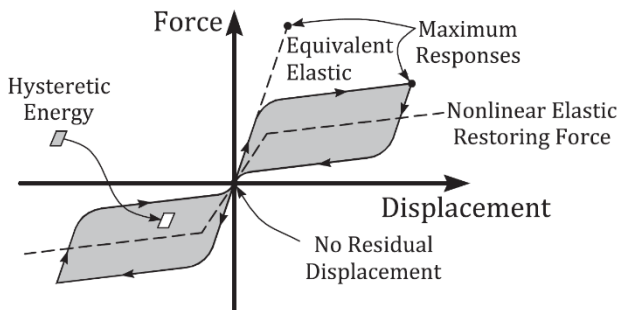


Figure 4 – Hysteretic behaviour of self-centring systems, adopted from Zhong et al. [16]

Several investigations were done to evaluate the seismic responses of SC-EBFs. Particularly, a SC-EBF with the use of rocking links and post-tensioned (PT) strands at the beam web was analysed by Cheng et al. [18]. The rocking characteristic of links is attained by separating the interface between the link and the adjacent beams. Under lateral loads, the PT strands ensure the

self-centring capacity of the frame while frictional hinge dampers at beam webs facilitate energy dissipation. Subsequently, Tong et al. [19] experimentally investigated the performance of a D-type SC-EBF with vertical or horizontal replaceable hysteretic damping (RHD) devices and PT bars. Results exhibited satisfactory self-centring ability of the SC-EBFs, and only plastic deformations were seen at the RHD devices which can be replaced easily. A similar study was done by Keivan et al. [20] on the seismic performance of K-type SCEBFs in which their self-centring abilities were confirmed. In 2016, Xu et al. [21,22] investigated a different approach by adopting the concept of including super-elastic shape-memory alloy (SMA) bolts and PT bars in EBFs. SMA is an alloy that can return to its re-deformed when exposed to an increase in temperature [23], hence promising excellent self-centring capacity and moderate energy dissipation. Garmeh et al. [24] conducted similar research on a SMA-based SC-EBF with links consisting of inner and outer components. These components are bolted to the adjacent beams using super-elastic SMA bolts. Under seismic accelerations, the inner link component can slide freely within the outer component to achieve self-centring in the frame. Nevertheless, the feasibility of including SMA devices proposed by Xu et al. and Garmeh et al. [21,22,24] in structures is restricted due to their limited application in the construction industry in recent years.

2.4 Damage-free Self-centring Links for Eccentrically Braced Frames by Lettieri et al.

2.4.1 Working Principle

This research focuses on evaluating a damage-free SC-link introduced by Lettieri et al. [5]. Figure 5 shows the SC-link proposed by Lettieri et al., which is pinned between two beams in an EBF. This device was designed for ultimate limit state and it aims at providing restoring force for EBFs while dissipating seismic energy in earthquakes by allowing the frame to oscillate during seismic events. The SC-link consists of a friction device (FD) which comprises a T-plate and two L-plates to produce I-shaped profile. Fiction pads are installed to the interfaces of the plates and pre-stressed by six high-strength bolts. Four PT-bars are post-tensioned symmetrically against anchor plate with disk springs installed at the ends to ensure the elastic behaviour of the bars. Figure 6 shows the deformed shape of the SC-EBF under horizontal acceleration. As the longitudinal shear force in the frame exceeds the friction force in FD (F_{FD}) and the initial post-tensioning force in the PT-bars (F_{PT}), gap-opening mechanism is generated at the pinned connections which rotates the link till a designed rotation (θ_p) of 0.08 rad. This rotation induces the elongation of PT-bars and longitudinal sliding within the friction device. Seismic energy is dissipated when the friction

pads in FD slide against each other. As the PT-bars elongate, the increase in tension forces in the PT bars and the compression forces developed in the disk springs induce a restoring force, providing the self-centring ability to the SC-link.

The behaviour of the SC-EBF can be demonstrated by plotting the longitudinal shear force subjected to the link over its displacement in Figure 7. The area under the flag-shape graph corresponds to the energy dissipation in the SC-EBF. It can be seen that the flag-shape graph does not intersect with the x-axis which implies that the SC-EBF exhibits no residual deformation. The increase in force between Point 1 and 2 on the graph represents the sum of the initial post-tensioning force in the PT-bars (F_{PT}) and friction force developed in the FD (F_{FD}). As the force subjected to the link exceeds Point 2, the PT-bars start to elongate and the FD slides till Point 3. At Point 3, the designed link rotation is reached, and the link begins to restore to its original position. The decrease in force between Point 4 and Point 5 represents the dissipated energy by the FD. At Point 5, the link is restored to its initial configuration with no residual displacement.

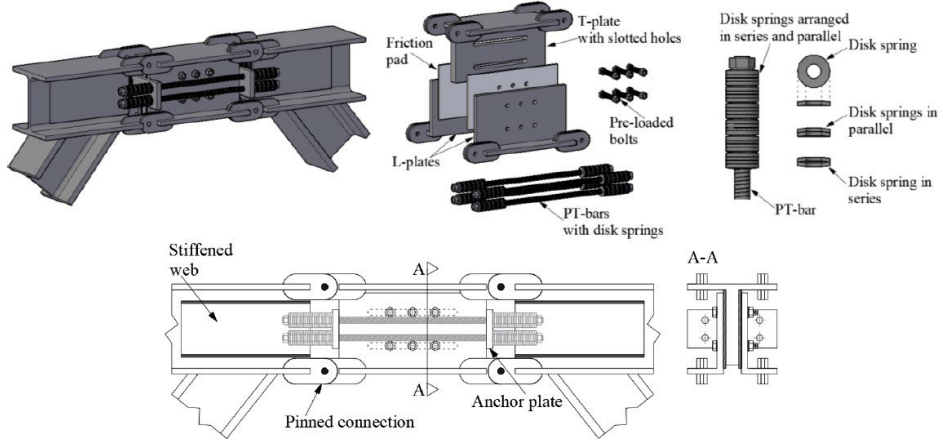


Figure 5 – Demonstration of the components in SC-link extracted from Lettieri et al. [5]

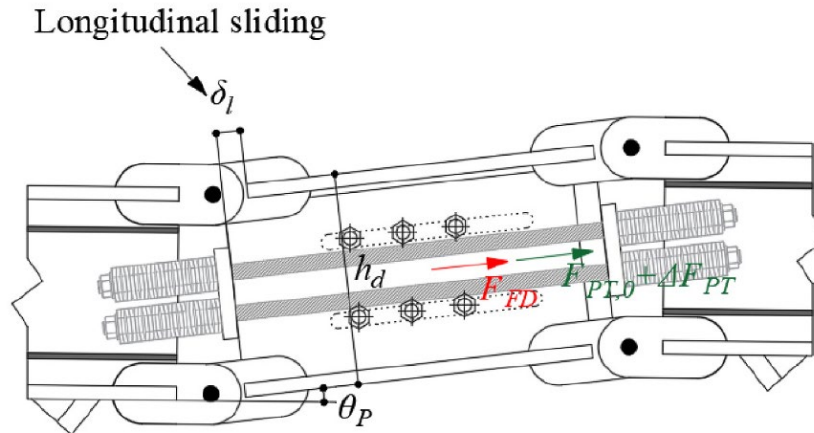


Figure 6 – Demonstration of a oscillating SC-EBF extracted from Lettieri et al. [5]

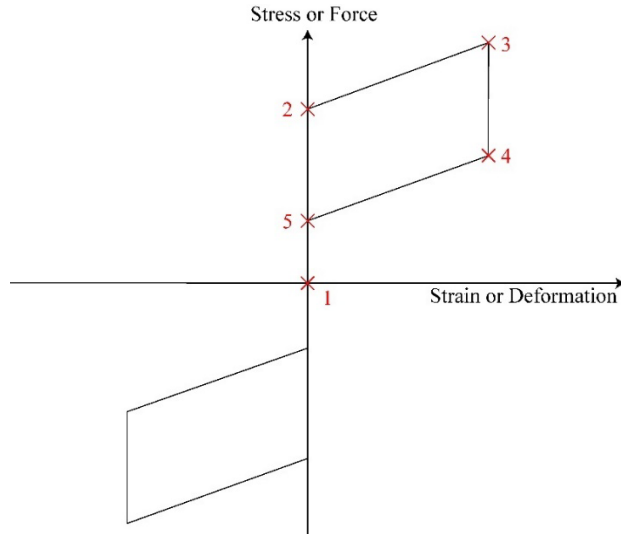


Figure 7 – Hysteretic longitudinal shear vs displacement graph showing point 1- 5

2.4.2 Exiting Study on Uncertainty Evaluation

Tubaldi et al. [25] previously examined the impact of model uncertainties on the seismic response of a steel-concrete composite bridge. To incorporate the model uncertainties into the structural analyses, they first identified the primary sources of such uncertainties. Then, they characterized the uncertainty parameters by determining the mean values and dispersion and representing them through Gaussian Distributions. Monte Carlo simulation was performed, which generated random values from the distributions and utilized them as input for the analyses. This enabled the analyses to account for the model uncertainties within the system.

Moderini [9] identified the two main sources of uncertainty in the SC-link: model uncertainties and ground motion uncertainties (record-to-record uncertainties). It was found that model

uncertainties arise from the friction coefficient in the friction device (μ), prestressing force in each bolt in FD ($F_{p,FD}$) and the post-tensioning force in each PT-bar ($F_{p,PT}$) respectively while ground motion uncertainties arise as structures respond differently to different ground motions. From Moderini's thesis, it was concluded that the mentioned uncertainties had a negligible impact on the SC-link's performance. However, this uncertainty evaluation study was done under the assumption that the ratio of total force in the PT bars (F_{PT}) to total friction force in the FD (F_{FD}) is always $\frac{0.6}{0.4}$. To improve the comprehensiveness of the uncertainty evaluation study, it would be advantageous to conduct additional investigation into the seismic responses of SC-link with varying $\frac{F_{PT}}{F_{FD}}$ ratios. Accordingly, this thesis presents the impact of uncertainties on the SC-EBF under different scenarios of $\frac{F_{PT}}{F_{FD}}$ ratios.

3 CASE-STUDY STRUCTURE AND FINITE ELEMENT MODELLING

3.1 Properties and Geometry

A case study of a four-storey, five-bays by three-bays steel residential building, as shown in Figure 8, was previously conducted by Lettieri et al. [5] to validate the seismic resilience of the SC-EBF. Since this building type is common in residential areas, it was deemed to be an appropriate choice for this research and thus the same case study structure was used. The building comprises two framing systems: self-centring K-type EBFs located in the central bay of the outermost frame in the x-direction, providing seismic resilience, and gravity frames located in the interior part. The beam-to-column connections and column base support conditions are pinned, and composite deck slab floors are used to ensure the overall stability of the structure. As seismic resistance is only provided by the SC-EBFs located at the outermost central bay, the case study was simplified by only focusing the outermost central bay of SC-EBF. This simplification allows for reduction in computational demand while analysing the dynamic response of the structure. The design details of the simplified one-bay, four-storey frame are summarised in Table 1, Table 2 and Table 3.

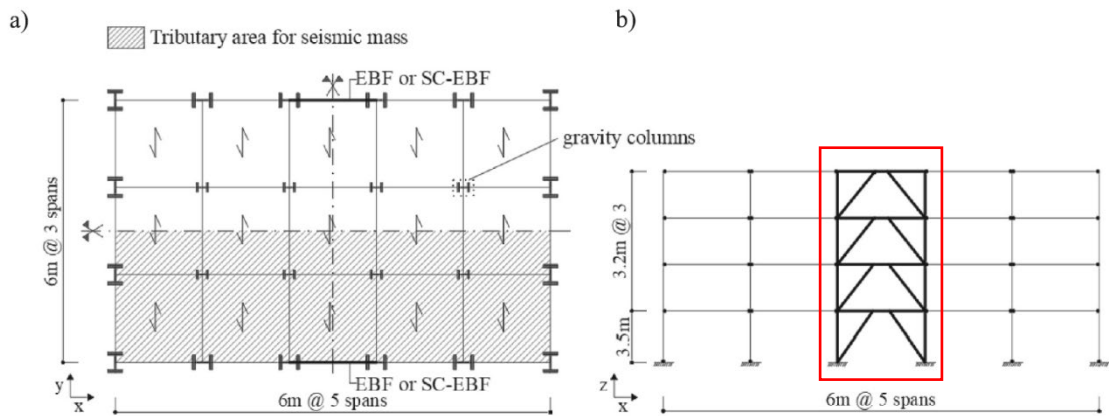


Figure 8 – 5x4 case-study frame adopted from Lettieri et al. [5]: (a) Plan view; (b) Elevation view

Table 1 – Design Summary of the simplified EBF adopted from Lettieri et al. [5]

Storey	Brace Section	Column Section	Link Section	Link Length, e [mm]
1 st	HE 240M	HE 320B	HE 360B	1100
2 nd	HE 220M	HE 320B	HE 320B	1000
3 rd	HE 200M	HE 280B	HE 280B	900
4 th	HE 180M	HE 280B	HE 200B	600

Table 2 – Design Summary of the SC-links adopted from Lettieri et al. [5]

Storey	Bolts	Bolt pre-load	PT-bars	PT-bar post-tension	K_{eq} SC-link
	[–]	[kN]	[–]	[kN]	[N/mm]
1 st	6 M22	135	4 M30	323	6899
2 nd	6 M20	113	4 M27	270	5490

3 rd	6 M18	90	4 M24	215	4434
4 th	6 M16	72	4 M20	115	5992

Table 3 – Section Properties of the SC-links adopted from Lettieri et al. [5]

	H [mm]	t _w [mm]	t _f [mm]	B [mm]	L [mm]	Steel Grade [-]
T-plate	252	40	18	280	810	S275
L-plate	252	20	18	280	810	S275
FDs shims	244	8	–	–	810	S275 (Thermally sprayed)

3.2 Finite Element Modelling

The extracted SC-EBF was developed as a 2D Finite Element Model (FEM) in Opensees. The Open System for Earthquake Engineering Simulation (Opensees) is a software framework for finite element analysis that simulates the seismic response of structural systems. It allows for carrying out nonlinear analysis to simulate the inelastic behaviour of materials during seismic events [26]. To define the structure's geometry and properties in Opensees, the TCL programming language is used.

Figure 9 shows the various options provided by Opensees for modelling the plasticity and nonlinear behaviour of a structure. The options fall into two main categories: Concentrated Plasticity and Distributed Plasticity. The comparison of these categories is presented in Table 4. In this study, the structural elements were modelled using “*Fibre Section*” as it allows for a more detailed analysis of the response in different sections along an element.

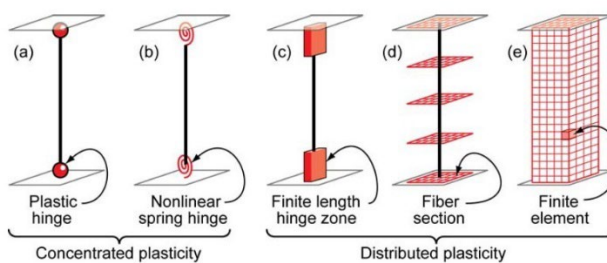


Figure 9 – Available options to model plasticity in Opensees extracted from Reinhorn et al. [27]

Table 4 – Comparison of plasticity models

	Concentrated Plasticity (Non-Linear Spring Hinge)	Distributed Plasticity (Fibre Section)
Inelastic Behaviour	<ul style="list-style-type: none"> Concentrated at the end of the element 	<ul style="list-style-type: none"> Distributed along the whole element
Modelling Method	<ul style="list-style-type: none"> Modelled as an inelastic spring 	<ul style="list-style-type: none"> Divided into discrete plane sections along the member length
Modelling Element	<ul style="list-style-type: none"> Elements in pure bending 	<ul style="list-style-type: none"> Elements in bending and compression
Computational Demand	<ul style="list-style-type: none"> Less computationally intensive 	<ul style="list-style-type: none"> More computationally intensive

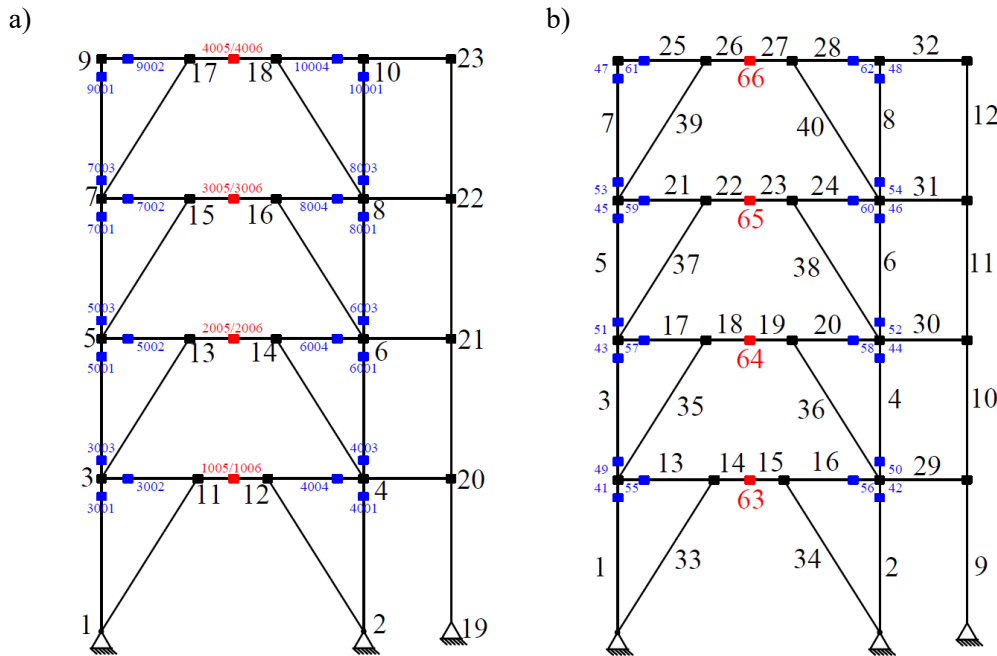


Figure 10 – (a) Positions of nodes and (b) Positions of elements of the simplified SC-EBF

Figure 10 demonstrates the geometry of the simplified SC-EBF model in Opensees, where Figure 10(a) indicates the positions of nodes and in Figure 10(b) annotates the elements.

Extra columns, named “*Leaning Columns*” were added into the simplified case-study model in Opensees to simulate the structural impacts of the remaining gravity frame components. Leaning columns are pinned at their base and connections. They do not contribute to a structure's seismic resistance, but to account for the P-Delta effects generated from the gravity frames. The leaning columns are modelled as “*elasticBeamColumn*” elements in Opensees and have stiffness and mass equivalent to the sums in the gravity frames. Figure 11(a) demonstrates the compositions of the simplified model.

Moreover, the beams, columns and bracings in the SC-EBF are modelled as “*nonlinearBeamColumn*”, using the “*Fibre Section*” approach to consider the plasticity along the element. “*WFsection*” and “*section Aggregator*” are also applied to the elements to better capture the local bending moment, shear and axial forces. The material properties of the beams, columns and bracings are modelled as “*Steel01*” material with 275 MPa yield strength. The non-linear behaviour of this material is defined by its yield strength, initial elastic modulus and the ratio between post-yielding stiffness and initial stiffness. The regions surrounding the rigid beam-column connections are defined as “*panel zones*” and annotated in Figure 11(b). Since “*panel zones*” are more rigid than other parts of the structure and are unlikely to undergo plastic deformation, it was assigned with the “*Elastic*” material, which is characterised with much higher strength than “*Steel01*”.

SC-link is modelled by having two “*nonlinearBeamColumn*” elements interconnected at mid-span via a non-linear vertical spring known as “*zeroLength*” element. The “*zeroLength*” element is modelled by defining two nodes at the same location to capture the transverse shear and deformation at the link’s mid-span. “*SelfCentering*” material, which has flag-shape behaviour, was assigned to the “*zeroLength*” element to assign the link with self-centring ability.

Four parameters are used to define the “*SelfCentering*” material property as illustrated in Figure 12 initial stiffness (k_1), post-activation stress (k_2), forward activation stress (sigAct) and ratio of forward to reverse activation stress (beta). The SC-link has a very high initial stiffness (k_1) tending to infinity due to its rigid-plastic behaviour before the gap-opening mechanism (elongation of PT-bars) occurs. Once this mechanism is activated, the link’s stiffness is defined by k_2 , which is the sum of PT-bar stiffness and disk spring stiffness. The value of “*sigAct*” is defined by the sum of F_{FD} and F_{PT} , while the height of the flag-shape loop, $\text{sigAct} \times \text{beta}$, is defined by $2F_{FD}$.

Additionally, to simulate the P-Delta effect which causes secondary moments due to the interaction of axial forces and deflections at the element ends, the majority of elements have to be assigned with a transformation property “*geomTransfPDelta*”.

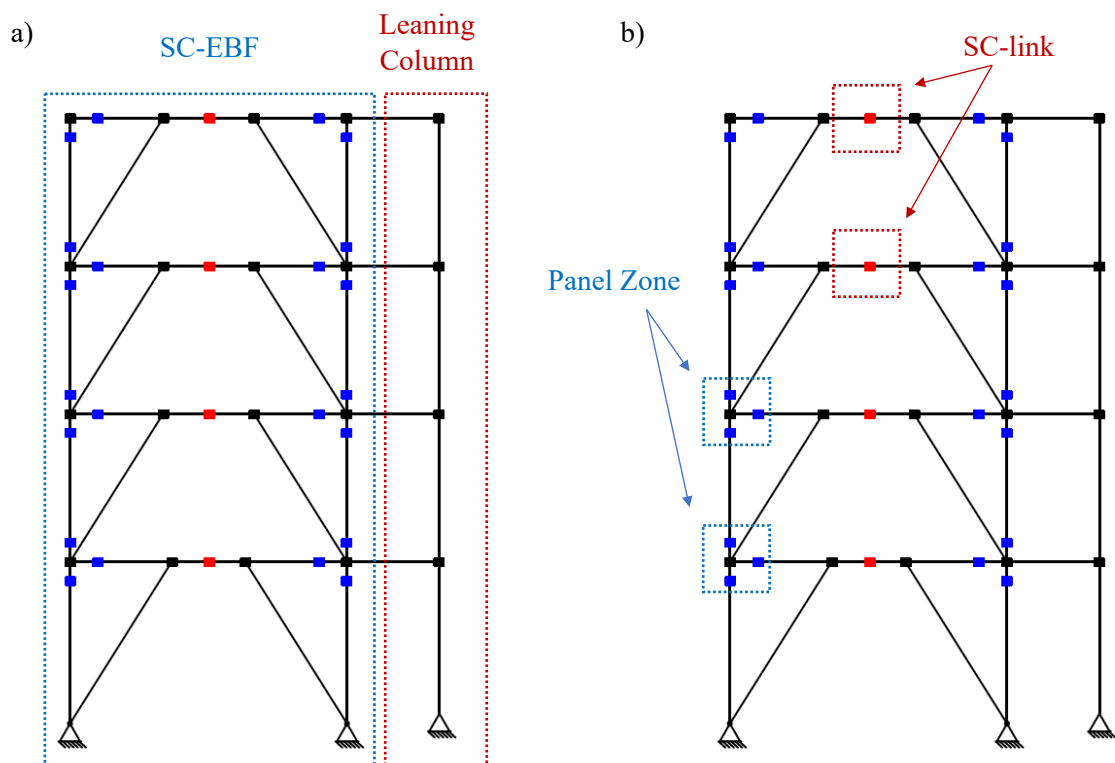


Figure 11 – Demonstration of the SC-EBF showing (a) Leaning columns, and (b) SC-link and Panel zone

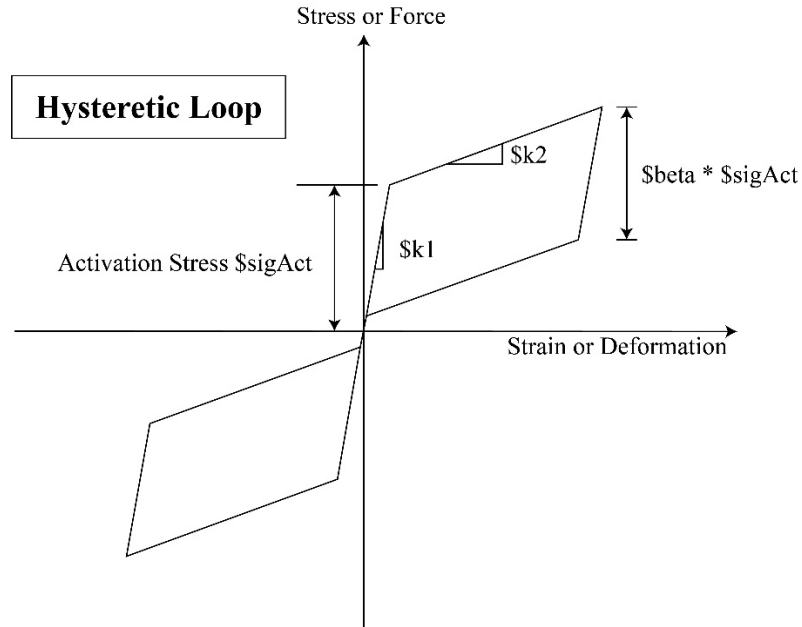


Figure 12 – General hysteretic loop showing parameters of “*SelfCentring*” materials, adopted from Jeff Erochko et al. [28]

4 PERFORMANCE ASSESSMENT FRAMEWORK

The evaluation of the SC-EBF's performance was carried out in two stages: firstly, in Section 4.1, by analysing the influence of uncertainties on seismic responses and resistance under different sets of $\frac{F_{PT}}{F_{FD}}$ ratios, and secondly, by determining the ideal equilibrium between its self-centring ability and energy dissipation capacity in Section 4.2.

4.1 Evaluation of Uncertainties

4.1.1 Classification of Uncertainty

There are two main types of uncertainties in the theoretical behaviour of the SC-EBF: (1) model uncertainties and (2) record-to-record uncertainties. Model uncertainties arise due to the imperfection in the fabrication of SC-links in real life, which causes discrepancies between the theoretical and practical behaviour of the links. Record-to-record uncertainties arise since structures behave differently under different ground intensities and the relationship between structural responses and intensities is not always linear.

Three main design parameters contribute to the uncertainties in the model: the dynamic friction coefficient (μ) and the preloading forces in each bolt of FD and each PT bar ($F_{p,FD}$ and $F_{p,PT}$). Dynamic friction coefficient (μ) is the ratio of friction force exerted on the FD to the normal force on the surface in contact. Different materials have different dynamic friction coefficients. Since it is impossible to ensure the consistency of the material quality of every FD, the friction coefficient of links may vary from each other. $F_{p,FD}$ and $F_{p,PT}$ are the resisting forces acting against the lateral seismic loads by preloading the PT-bars and FDs. Since it is difficult to load the PT-bars and bolts to the exact designed values, uncertainties arise.

The British Standard [29] and a study by Latour et al. [30] suggested that the variability in the values of μ , $F_{p,FD}$ and $F_{p,PT}$ can be described by normal distributions, which are characterised by two parameters: the mean and standard deviation. The mean values and coefficients of variation (COV) of μ , $F_{p,FD}$ and $F_{p,PT}$ are summarised in Table 5. The standard deviation of each variable can be calculated from COV which is the ratio of standard deviation to its mean value. Thus, normal distributions of μ , $F_{p,FD}$ and $F_{p,PT}$ of each storey can be obtained and shown in Figure 14.

Table 5 – Coefficient of variation (COV) of μ , $F_{p,PT}$ and $F_{p,FD}$

Parameters	COV
μ	0.08 [30]
$F_{p,FD}$	0.06 [29]
$F_{p,PT}$	0.06 [29]

4.1.2 Implementation of Monte Carlo Simulation

To assess the impact of uncertainties on the SC-EBF, seismic responses are recorded for two scenarios: one with uncertainties and one without. A comparison of these responses is conducted to determine whether a notable difference exists between them.

To account for record-to-record uncertainties that may lead to variations in SC-EBF performance in both scenarios, 240 sample cases are generated in each scenario using a set of 240 ground

motions prepared by Jayaram et al., as demonstrated in Figure 13 [31]. This results in 240 cases for each scenario.

The scenario without uncertainties is simulated by modelling the SC-EBF with the mean values of μ , $F_{p,FD}$ and $F_{p,PT}$. The scenario with uncertainties is modelled using various sets of μ , $F_{p,FD}$ and $F_{p,PT}$ selected from their respective normal distributions. Monte Carlo Simulation, a random number generator, is used to generate these sets of random samples from the given distributions [32].

Figure 14 illustrates an example of Monte Carlo Simulation in one of the scenario cases. In Figure 14(a), 240 values of μ are selected from its distribution, each corresponding to one of the 240 loading cases. Each loading case should have 6x4 (i.e., 24) $F_{p,FD}$ since there are six bolts in a single FD and each of the four storeys in the SC-EBF has an FD. Thus, a total of 24x240 (i.e., 5760) $F_{p,FD}$ values are chosen for the 240 loading cases, as shown in Figure 14(b). Additionally, since each SC-link has four PT-bars, and there is one SC-link in each of the four storeys, each of the 240 sample cases should contain 4x4 (i.e., 16) sets of $F_{p,PT}$, leading to a total of 16x240 (i.e., 3840) magnitudes of $F_{p,PT}$ for the 240 loading cases as shown in Figure 14(c).

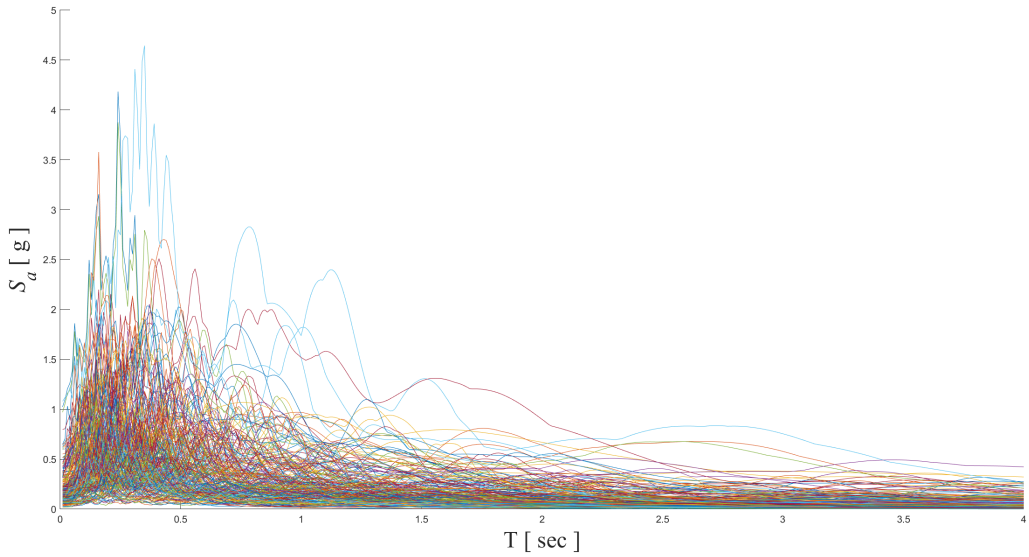


Figure 13 – A set of 240 ground motions adopted from Jayaram et al. [31]

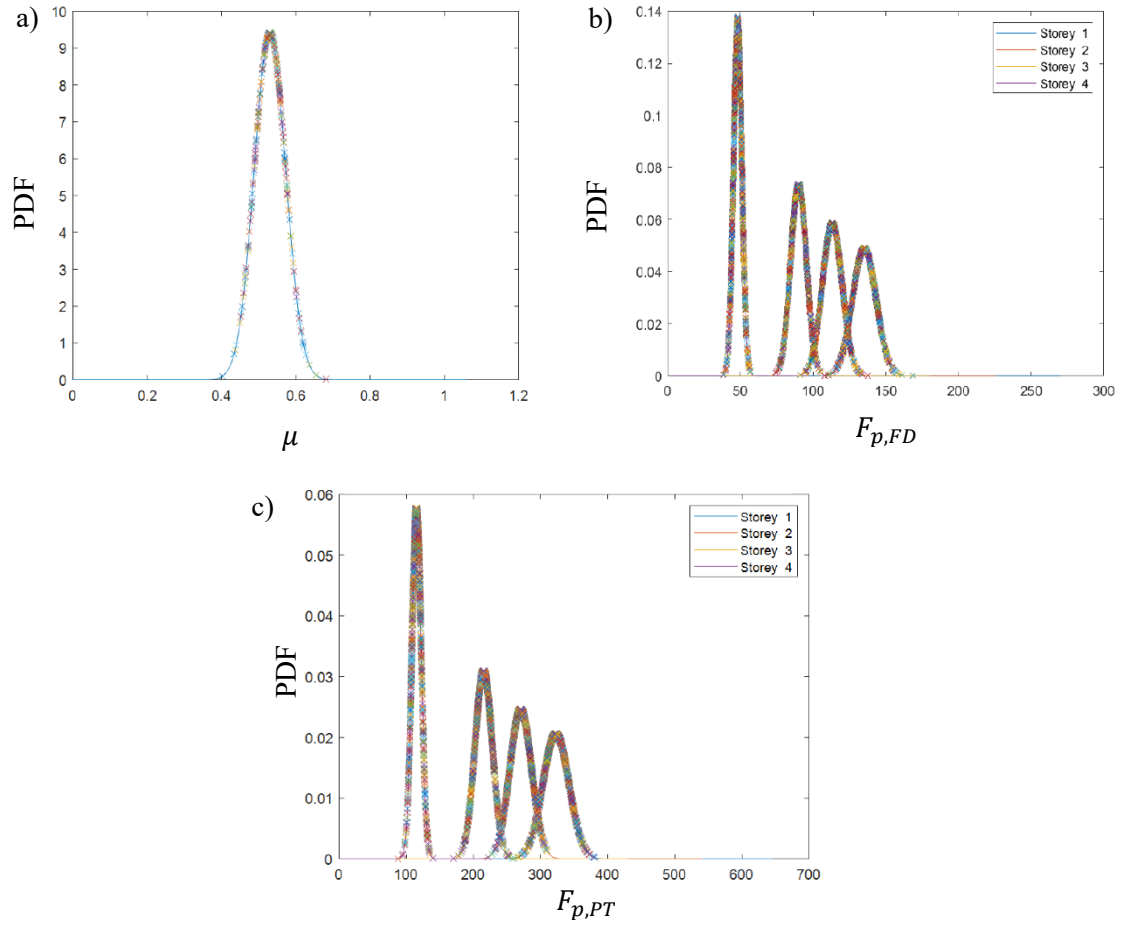


Figure 14 – Distributions of μ , $F_{p,PT}$ and $F_{p,FD}$ of SC-links on each storey and sample selection by Monte Carlo Simulation: a) sample selection of μ ; b) sample selection of $F_{p,PT}$; c) sample selection of $F_{p,FD}$

4.1.3 Computation of the Hysteretic Behaviour of SC-link

According to the literature review, the behaviour of SC-links follows a flag-shaped hysteretic loop to prevent residual deformations after unloading. However, uncertainties in the SC-link model can affect this behaviour and the flag-shaped pattern may not be guaranteed. To assess the impact of uncertainties on the hysteretic behaviours of SC-links, computations were carried out to determine the hysteretic loops of SC-links modelled with nine different sets of $\frac{F_{PT}}{F_{FD}}$ ratios.

Before modelling and analysing the SC-link, parameters that demonstrate the structural behaviour of the frame should be calculated from analytical equations obtained from literature (Lettieri 2023). Figure 15 displays the deformed shape of a one-storey SC-EBF while Figure 16 illustrates the internal forces in SC-link under shear force (F). From the force diagram, the SC-link is subjected to transverse shear forces (V) along z-direction, bending moments (M) along its length and longitudinal shear forces (F_l) along x-direction. These forces are given by

$$V = \frac{F \times H}{L} \quad (1)$$

where H is the storey height and

L is the span of the frame.

$$M = V \times \frac{e}{2} \quad (2)$$

where e is length of the SC-link.

$$F_l = 2 \times \frac{M}{h_d - t_f} \quad (3)$$

where h_d is the section height of the link,

t_f is flange thickness.

The friction force in the FD (F_{FD}) which governs the energy dissipation capacity of the frame is given by

$$F_{FD} = \mu \times n_s \times n_b \times F_{p,FD} \quad (4)$$

where μ is the friction coefficient of the FD,

n_s is the number of friction interfaces,

n_b is the number of bolts,

$F_{p,FD}$ is the preloading force in each bolt of FD.

The post-tensioning force in the PT-bars (F_{PT}) which governs the self-centring behaviour of the SC-link is given by

$$F_{PT} = n_{PT} \times F_{p,PT} \quad (5)$$

where n_{PT} is the number of PT-bars in the SC-link,

$F_{p,PT}$ is the post-tensioning force of each of the four PT-bars in the SC-link.

By utilising equation 1-3, the longitudinal shear forces, F_{PT} and F_{FD} , are transformed into transverse shear forces V_{PT} and V_{FD} . The four transverse shear forces (i.e., V_1, V_2, V_3, V_4) that define the hysteretic loop of SC-links are shown in Figure 17. They are formulated as

$$\begin{aligned} V_1 &= V_{PT} + V_{FD} \\ V_2 &= V_1 + \Delta V_{PT} \\ V_3 &= V_2 - 2V_{FD} \\ V_4 &= V_3 - \Delta V_{PT} \end{aligned} \quad (6)$$

where ΔV_{PT} is the increase in force in the PT-bars due to elongation.

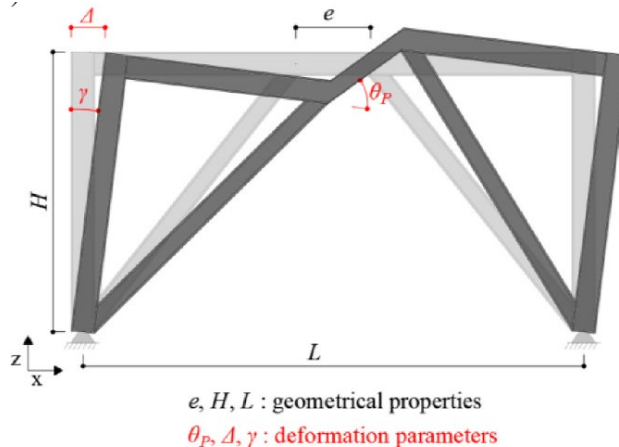


Figure 15 – Deformed shape of SC-EBF adopted from Lettieri et al. [5]

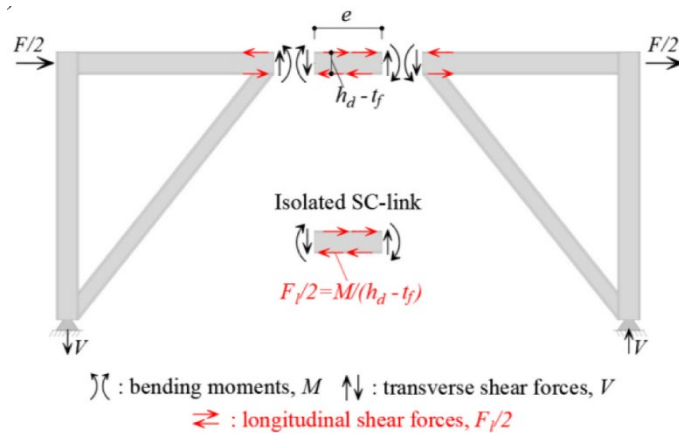


Figure 16 – Free-body diagram of the forces acting on SC-EBF adopted from Lettieri et al. [5]

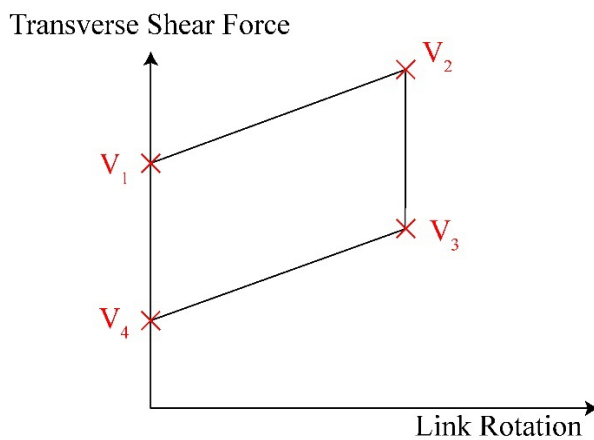


Figure 17 – Transverse shear force (V) vs. link rotation (θ) graph with V_1, V_2, V_3, V_4 defined

4.1.4 Cloud Analysis

Cloud Analysis is a well-known procedure of constructing linear regression models in logarithmic scale for structural response and ground motion intensity. This method was widely used in previous studies due to its simplicity. In this research, Cloud Analysis is used to establish the correlations between engineering demand parameters (EDP) and intensity measures (IM) under various scenarios. The definition of EDP and IM will be discussed in Section 4.1.4.2.

As noted in the literature review, an uncertainty evaluation study is preliminary conducted by Moderini [9] on a SC-link which is characterised by $\frac{F_{PT}}{F_{FD}} = \frac{0.6}{0.4}$. Building upon that, this research delved further into investigating the impact of SC-link uncertainties on SC-EBF by exploring the difference in frame performance between scenarios with uncertainties and without uncertainties in terms of nine $\frac{F_{PT}}{F_{FD}}$ ratios (Table 6).

Table 6 – 9 sets of $\frac{F_{PT}}{F_{FD}}$ ratios considered in the cloud analysis

	1	2	3	4	5	6	7	8	9
F_{PT}	0.10	0.20	0.30	0.40	0.50	0.60	0.70	0.80	0.90
F_{FD}	0.90	0.80	0.70	0.60	0.50	0.40	0.30	0.20	0.10

The comparison of seismic behaviours between scenarios with and without uncertainties of each $\frac{F_{PT}}{F_{FD}}$ ratio case is conducted firstly in terms of a) hysteretic behaviour, b) engineering demand parameters and c) fragility analyses. Before comparisons can be done, various analyses were done to capture the dynamic responses of the frame when subjected to earthquake. The analyses conducted will be explained in detail in the following sections.

4.1.4.1 Numerical Analyses in OpenSees

Several analyses were conducted in OpenSees to obtain the dynamic structural response of the SC-EBFs:

a) Modal Analysis

Modal analysis refers to the procedure of obtaining modal parameters, such as period of the fundamental frequency (T_1) of the SC-EBF, the Rayleigh Damping mass coefficients (α) and the Rayleigh Damping stiffness coefficients (β) [33]. The direct outputs from modal analysis are in terms of eigenvalues and eigenvectors. It is worth noting that the outputs contain four sets of eigenvectors and eigenvalues, each representing different modes of vibration and the first set represents the fundamental vibration. The sets of eigenvalues are then converted to period of vibration with the following set of equations:

$$\left\{ \begin{array}{l} \text{Eigenvalue} = \omega_i^2 \\ T_i = \frac{2\pi}{\omega_i} \end{array} \Rightarrow T_i = \frac{2\pi}{\sqrt{\text{Eigenvalue}}} \right. \quad (7)$$

where T_i is the vibration period of different modes,

ω_i is angular frequency of different modes.

The Rayleigh damping coefficients (i.e., α and β) are determined as follows [34]:

$$\alpha = \frac{2\omega_1\omega_2}{\omega_2^2 - \omega_1^2} (\omega_2\xi_1 - \omega_1\xi_2) \quad (8)$$

$$\beta = \frac{2}{\omega_2^2 - \omega_1^2} (\omega_2 \xi_2 - \omega_1 \xi_1) \quad (9)$$

where ξ_1, ξ_2 are damping ratios, assumed to be 0.03 (3% viscous damping)

The obtained T_1 is used in defining IMs, $S_a(T_1)$, in this study. On the other hand, Rayleigh Damping coefficients (i.e., α and β) are used to model the dissipation of internal energy in the SC-EBF, which is caused by internal friction that occurs under accelerations [35]. This is helpful in creating a mathematical model for dynamic analyses of the frame subsequently.

b) Dynamic Analysis

Dynamic analysis was conducted to simulate the seismic response of the SC-EBF when it was subjected to the 240 ground motions as illustrated in Figure 13. In OpenSees, the “*UniformExcitation pattern*” command was used to apply the ground motions to all the nodes in the SC-EBF, and the timestep and x-direction of the ground motions were specified within the command.

The definition of analysis options involved multiple steps. Firstly, constraints were imposed by creating a multi-point constraint handler using the “*Transformation Constraint*” command, which relied on the transformation equation method. Next, damping was assigned to all the elements in the SC-EBF using the “*Rayleigh Damping*” command to model the energy dissipation in the structural elements due to internal friction. The “*Rayleigh Damping*” command was set by defining the “*alpham*” and “*betak*” of the SC-EBF obtained from the modal analysis discussed in the previous section. These values correspond to the factors that were applied to mass and stiffness of elements and nodes respectively.

Several recorders were set at different structural parts of the SC-EBF. “*Node Recorder*” command was set at nodes 4, 6, 8, 10 illustrated in Figure 10 to record the frame sway displacements at storey 1, 2, 3, 4. The base reactions of the SC-EBF was captured by setting “*Node Recorder*” command at supports (i.e., nodes 1, 2, 19). “*Element Recorder*” command was assigned to all the beams, diagonals, links and columns to record their reaction forces and deformations. Specifically, the frame sway displacements recorded at the storey’s nodes were used to calculate the engineering demand parameters specified in the following section.

4.1.4.2 Earthquake Intensity Measures and Engineering Demand Parameters

The key features of ground motion that affect the structural responses of structural frames are described by Intensity Measures (IMs) [36]. For this study, the selected 240 ground motions are characterised by spectral accelerations at the first-mode period i.e., $S_a(T_1)$. T_1 corresponds to period of the fundamental frequency of the SC-EBF which is obtained from the modal analysis outlined in Section 4.1.3.1a). $S_a(T_1)$ is measured with respect to the gravitational acceleration of Earth, g . The range of $S_a(T_1)$ in this study is from 0 g to 2.5 g .

The seismic responses under 240 sets of $S_a(T_1)$ are captured in terms of three engineering demand parameters (EDPs) which are quantities that describe the response of a SC-EBF in ground motions [36], including peak interstorey drift ratios (IDR_{peak}) and peak link rotations (θ_{peak}) and residual interstorey drift ratios (IDR_{res}).

IDR_{peak} is expressed as a percentage and represents the maximum ratio of the horizontal displacement between two consecutive floors to the height of one storey in the SC-EBF. It is formulated as

$$IDR_{peak}(\%) = \frac{\Delta_{max}}{H} \times 100\% \quad (10)$$

Where Δ_{max} is the maximum frame sway displacement recorded from the dynamic analysis outlined

in Section 4.1.3.1b),

H is the storey height.

θ_{peak} is expressed in radians and represents the maximum rotation of the SC-link. It is formulated as

$$\theta_{peak}(rad) = \frac{\Delta_{max}}{H} \times \frac{L}{e} \quad (11)$$

Where L is the span of the frame,

e is the span of the link.

IDR_{res} is defined as the ratio of remaining interstorey drift in the SC-EBF after unloading to the storey height. It is expressed in percentage and formulated as

$$IDR_{peak}(\%) = \frac{\Delta_{res}}{H} \times 100\% \quad (12)$$

where Δ_{res} is the residual frame sway displacement after the SC-EBF is unloaded. It is also recorded from the dynamic analysis outlined in Section 4.1.3.1b),

Each engineering demand parameter has its respective capacity beyond which the SC-EBF will be considered as unstable and irreparable. Eurocode 8 [2] specifies that for short links, the rotation angle should not exceed 0.08 radians. In addition, according to the uncertainty analysis of SC-link by Moderini [9], the peak interstorey drift ratio (IDR_{peak}) should not exceed a threshold of 2%.

Several studies have identified the permissible residual deformation levels in EBFs. From a study of residual drifts of 12 steel frames conducted by Iwata et al. [37], it was concluded that the overall residual drifts of structures should not exceed 0.005 rad or else repairing will be non-economical. McCormick et al. [38] further corroborated this finding by recommending a drift limit of 0.005 radians after considering functionality, construction tolerances, and safety. FEMA P-58 [39] suggested two damage states for residual interstorey drift ratio: Damage State 1 (DS1) and Damage State 2 (DS2), with thresholds of 0.2% and 0.5% respectively. DS1 corresponds to damage condition where structural realignment is not necessary before repair, while DS2 requires major realignment, making repairs uneconomical. In this study, thresholds of DS1 (0.2%) and DS2 (0.5%) were used to justify the seismic resilience of the SC-EBF.

The threshold capacities of IDR_{res} , IDR_{peak} and θ_{peak} are summarised in Table 7.

Table 7 – Threshold capacities of IDR_{peak} , θ_{peak} and IDR_{res}

	IDR_{peak}	θ_{peak}	IDR_{res}
Threshold Capacities	2%	0.08 rad	DS1: 0.2%
			DS2: 0.5%

4.1.4.3 Linear Regression

Linear regressions were conducted to visualise the impact of uncertainties on IDR_{peak} and θ_{peak} . According to the probabilistic framework for seismic assessment of structures proposed by Cornell et al. [40], relationship between seismic demand (D) and capacity (C) is as follows:

$$D = a(S_a)^b \quad (13)$$

By taking natural logarithm on both sides of equation 13, a linear function in terms of D and C was produced:

$$\ln(D) = b \times \ln(Sa) + \ln(a) \quad (14)$$

in which D corresponds to IDR_{peak} and θ_{peak} .

By conducting regression analyses of $\ln(IDR_{peak})$ and $\ln(Sa)$, and, $\ln(\theta_{peak})$ and $\ln(Sa)$, on cases considering uncertainties and those that do not, the regression lines of both scenarios were drawn. If the regression lines of both scenarios overlap, it implies that the impact of uncertainties on the EDPs can be deemed as negligible.

4.1.4.4 Performance-based Fragility Analysis

Fragility analysis is a statistical tool that visualises the likelihood of exceeding a particular damage level as a function of engineering demand parameter [41]. In this study, fragility analysis was performed on IDR_{res} . This was done by using logistic regression which is a classification model that predicts for a binary outcome such as success or failure [42]. In other words, in this study, logistic regression models were used to estimate the probability of IDR_{res} exceeding its threshold capacities at a given IM (i.e., $S_a(T_1)$).

With the capacities of IDR_{res} listed in Table 7 and the resulting IDR_{res} obtained from dynamic analyses, each simulation case was classified into two classes: “success” or “failure”. The cases with IDR_{res} exceeding capacity were classified as “failure” while others were classified as “success”. With this binary classification, logistic probability function is applied to provide a generalised trends and estimate the failure probability at any given IM. The logistic probability function can be expressed as follows [43]:

$$P(Y = 1 | S_a(T_1)) = \frac{1}{1 + e^{(\beta \times S_a(T_1) + c)}} \quad (15)$$

where P is the probability of failure,

$S_a(T_1)$ is the first-mode spectral acceleration which is the intensity measure

β, c are the model coefficients.

By calculating the model coefficients in equation 15 with MATLAB, the fragility curve showing the likelihood of failure at any given IM can be established.

4.2 Optimisation of SC-link Model

As previously discussed in literature, the primary purpose of the SC-link is to protect the frame from irreversible deformation. This is achieved through the combined effect of energy dissipation from the FD device and self-centring abilities from the PT-bars. To optimise the SC-link's seismic performance, the goal is to maximise energy dissipation while also preventing any residual deformation of the frame after seismic events. This requires finding the optimal balance between friction force (F_{FD}) in the friction device and post-tensioning force (F_{PT}) in the PT-bars, which is determined by the $\frac{F_{PT}}{F_{FD}}$ ratio.

In this study, a set of 30 natural ground motion records prepared by Vamvatsikos et al. [40] were selected to aid the analysis of SC-link to find how different EDPs vary in different $\frac{F_{PT}}{F_{FD}}$ ratios to find the optimal ratio. The inclusion of these ground motions help eliminating the impact of record-to-record uncertainties in the analyses. As noted in Lettieri et al. [5]'s research, the SC-link was designed to meet the ultimate limit state (ULS) requirement, which ensures the SC-EBF can withstand the maximum allowable load for structural stability and safety. Thus, the link's performance is evaluated based on its seismic response at ULS intensity. The spectral acceleration at fundamental period of selected accelerograms are scaled at ULS intensity of $1.2\ g$, i.e., $S_a(T_1)_{ULS} = 1.2g$ [5].

Figure 18 shows the 30 selected accelerograms and the scaled spectrum at ULS intensity. Then, the $\frac{F_{PT}}{F_{FD}}$ ratio in the SC-link was varied from $\frac{0.10}{0.90}$ to $\frac{0.90}{0.10}$ and the EDPs under the 30 scaled accelerograms were found. The resulting IDR_{peak} , θ_{peak} and IDR_{res} of the 30 accelerograms were plotted against the $\frac{F_{PT}}{F_{FD}}$ ratios to visualise the trend of EDPs under different force ratios. The trends allow for easy evaluation of SC-link's performance under $\frac{F_{PT}}{F_{FD}}$ ratio, facilitating the identification of the best ratio.

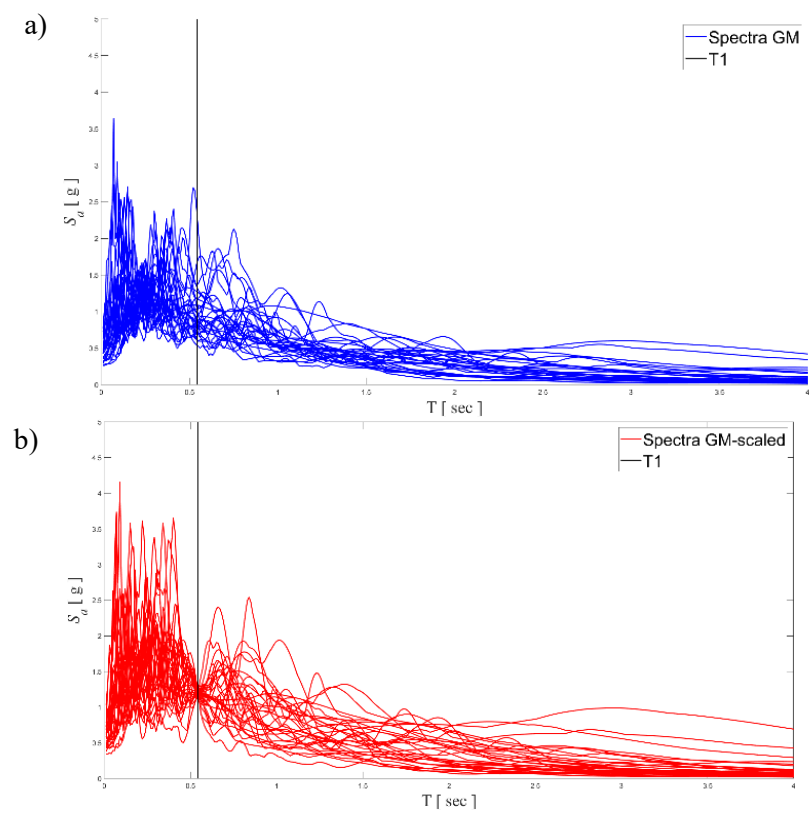


Figure 18 – a) Accelerograms of the selected 30 ground motions; b) Accelerograms scaled at the ULS intensity

5 RESULTS AND DISCUSSION

5.1 Impact of Uncertainties on SC-EBF

This section will evaluate the performance of the SC-EBF in two scenarios - one with uncertainties considered and the other without. The assessment will cover various aspects, including the local responses of the SC-link in terms of its hysteretic behaviours, and the engineering demand parameters, including peak interstorey drift ratio, peak link rotation, and residual interstorey drift ratio. The peak interstorey drift ratio and peak link rotation will be evaluated using regression analysis, while fragility analysis will be employed to evaluate the residual interstorey drift ratio.

The discussion of the results will focus on the seismic responses at storey 4 of the SC-EBF since it was found to have the highest deformation among all the storeys, making them the critical responses.

5.1.1 Hysteretic Behaviour

5.1.1.1 Hysteretic Loop

Figure 20 illustrates the hysteretic behaviour of SC-EBF with different $\frac{F_{PT}}{F_{FD}}$ ratios in terms of transverse shear force (V) vs. link rotation (θ). Each graph in Figure 20 was plotted by superimposing the hysteretic loops of 240 cases that take uncertainties into account with 240 cases that do not. As noted in the literature review of the SC-link, the area enclosed in the hysteretic loop indicates the dissipated energy, while the point where the loop intersects with the x-axis signifies the residual rotation in the link after unloading. It can be derived from the graphs that the hysteretic loop of each case does not overlap with the others, revealing that the introduction of uncertainties in the SC-link causes differences in structural behaviour, particularly in terms of self-centring ability and energy dissipation capacity. Taking the scenario $\frac{F_{PT}}{F_{FD}} = \frac{0.50}{0.50}$ as illustration in Figure 19, it can be seen that when no uncertainties were considered in the SC-link, the transverse shear force returns to zero after the frame is unloaded, implying that the frame does not experience any residual deformation. However, as uncertainties were included in the model, the resulting hysteretic loops vary from case to case, the non-overlapping loops caused by uncertainties make the loop intersect with the x-axis at a higher value. This suggests that uncertainties have led to higher residual rotations in the link, which in turn worsen its seismic resistance to earthquakes.

Additionally, it can also be observed that as $\frac{F_{PT}}{F_{FD}}$ increases, areas enclosed in the loops decrease which indicates lower energy dissipation. The graphs also show a reduced inclination of intersecting with the x-axis, indicating a decrease in residual link rotation. These observations align with the theoretical behaviour of the SC-EBF where at higher $\frac{F_{PT}}{F_{FD}}$ ratios, the post-tensioned force applied to the PT-bars is greater which results in more effective recentring of the frame. Simultaneously, less force is distributed to the FD so less energy is dissipated.

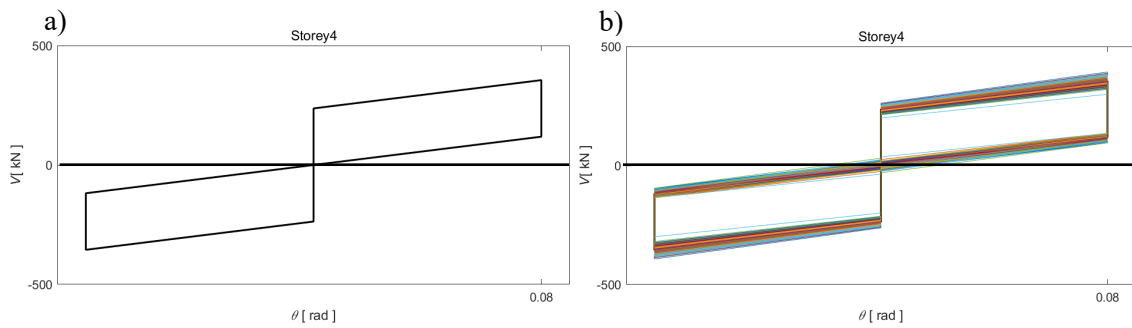


Figure 19 – Comparison of hysteretic loops at $\frac{F_{PT}}{F_{FD}} = \frac{0.50}{0.50}$ between a) cases without uncertainties and b) cases with uncertainties

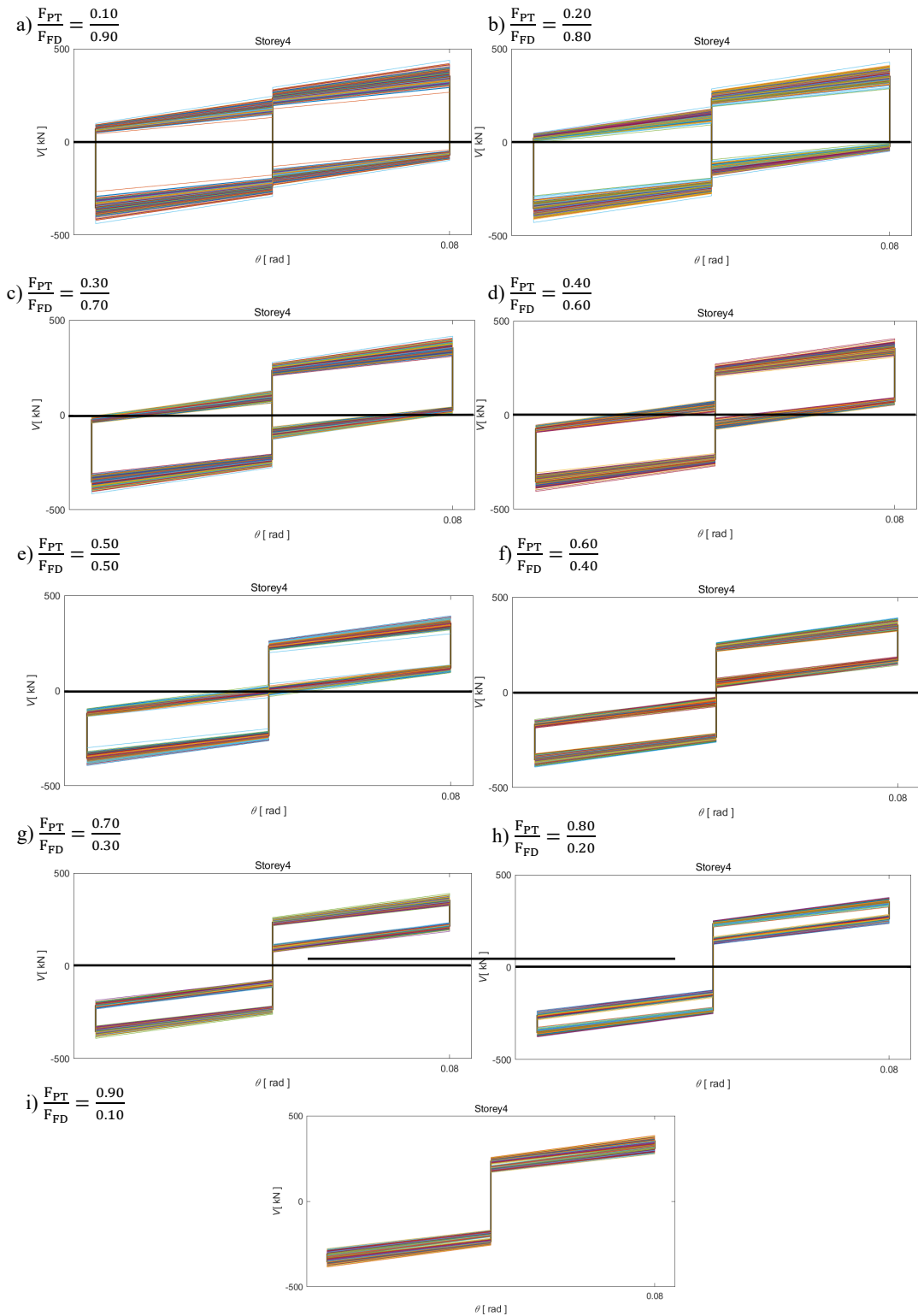


Figure 20 – Transverse shear force (V) vs. link rotation (θ) graphs of storey 4 of SC-EBF as $\frac{F_{PT}}{F_{FD}}$ varies from $\frac{0.10}{0.90}$ to $\frac{0.90}{0.10}$

5.1.2 Engineering Demand Parameters

5.1.2.1 Peak Interstorey Drift Ratio

The global responses of the SC-EBF can be observed in terms of peak interstorey drift ratio (IDR_{peak}) of the frame under various ground accelerations. Figure 22 displays nine graphs of IDR_{peak} vs. spectral acceleration ($S_a(T_1)$) at storey 4 of SC-EBF, with ratios of F_{PT} to F_{FD} ratios varying from $\frac{0.10}{0.90}$ to $\frac{0.90}{0.10}$. It is noticeable that, as expected, the IDR_{peak} values increase as $\frac{F_{PT}}{F_{FD}}$ ratios increase. This is because F_{FD} , which determines the energy dissipation capacity in the link, decreases as the $\frac{F_{PT}}{F_{FD}}$ ratio increases. The graphs also exhibit a relatively linear relationship between IDR_{peak} and $S_a(T_1)$, which disagrees with the theoretical behaviour of the frame. As evidenced by the hysteretic curves in Figure 19, force-deformation curve should exhibit backbone behaviour, which involves a change in gradient at higher force level. As acceleration is directly proportional to force, the change in gradient should also be visible in the graph of IDR_{peak} vs. $S_a(T_1)$, as demonstrated in Figure 21. The absence of change in gradient in the resulting graphs might be attributed to the limited sample size available within range of $S_a(T_1)$ between $1g$ and $2.5g$. Hence, the non-linearity of the curve could not be captured at that region.

To further discuss the agreement of IDR_{peak} values between the cases with uncertainties and cases without uncertainties, linear regression analyses were conducted on IDR_{peak} of different $\frac{F_{PT}}{F_{FD}}$ scenarios. Figure 23(a) shows the resulting regression graphs which include regression lines of the data points and the dispersion lines representing 95% confidence interval. The regression graphs from the 240 cases with uncertainties (red) are superimposed with those without uncertainties (blue). It can be noted that despite the difference between the red and blue data points are quite obvious in the IDR_{peak} vs. $S_a(T_1)$ graphs from Figure 22, the regression analyses show almost identical regression lines and confidence intervals for both red and blue cases. Hence, it can be concluded that the impact of uncertainties on the magnitude of IDR_{peak} is negligible.

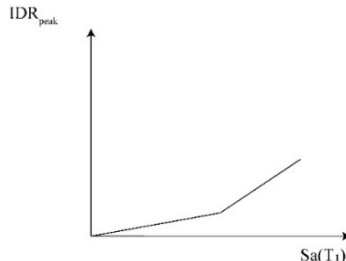


Figure 21 – Theoretical relationship between peak interstorey storey drift ratio (IDR_{peak}) and spectral acceleration ($S_a(T_1)$)

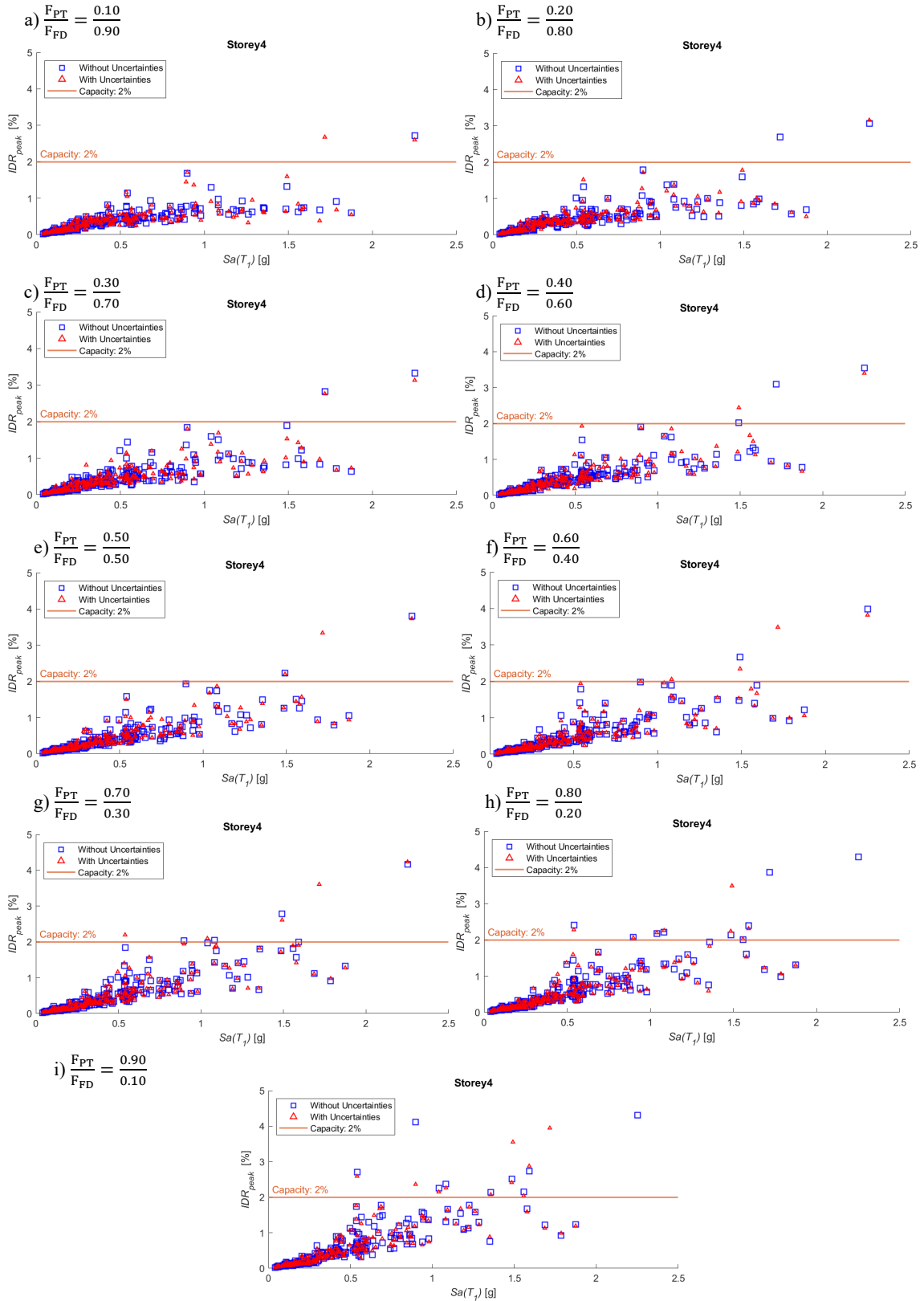


Figure 22 – Plots of peak interstorey drift ratios (IDR_{peak}) at storey 4 of SC-EBF under accelerations as

$$\frac{F_{PT}}{F_{FD}} \text{ varies from } \frac{0.10}{0.90} \text{ to } \frac{0.90}{0.10}$$

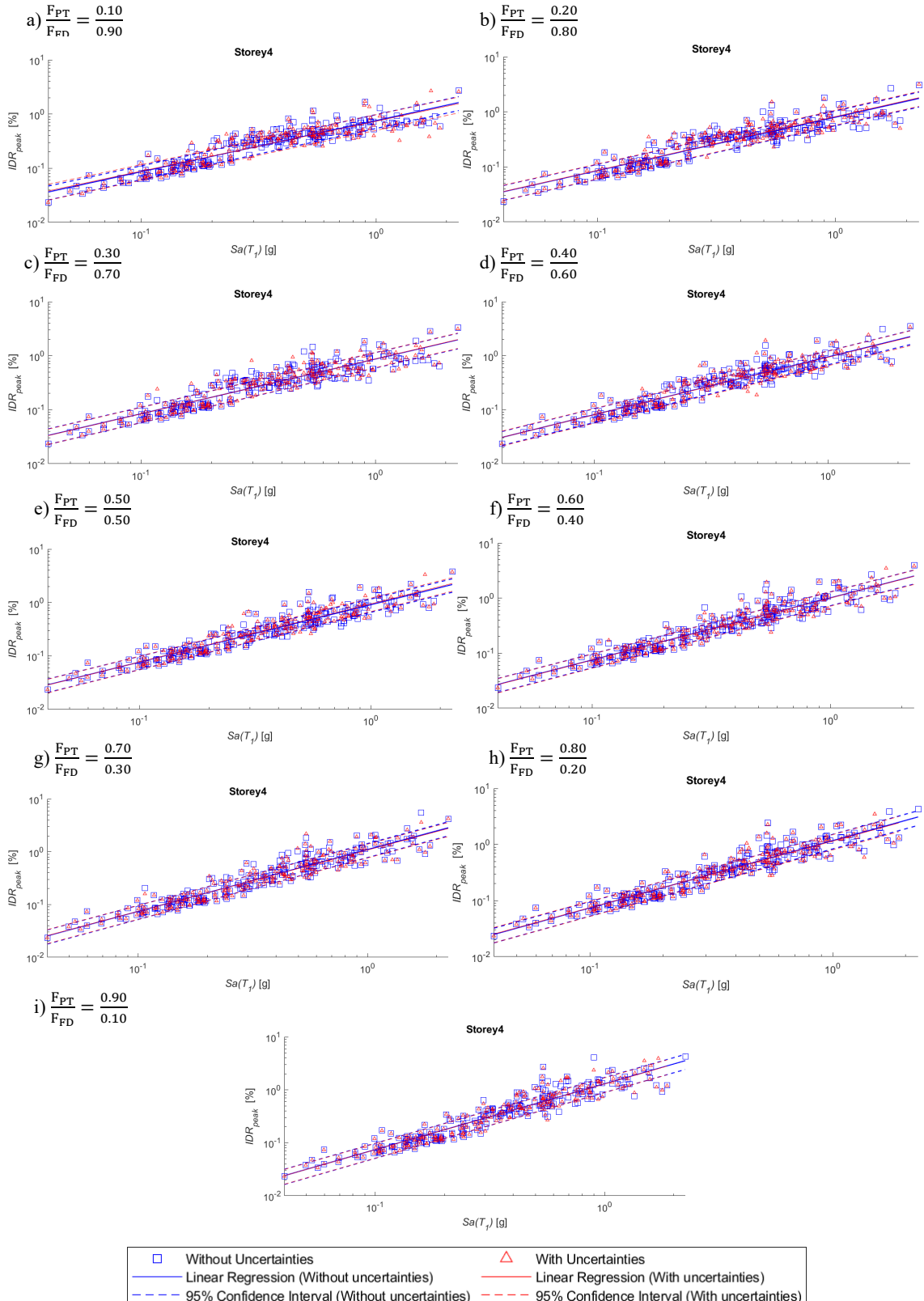


Figure 23 – Linear regression of peak interstorey drift ratios (IDR_{peak}) at storey 4 of SC-EBF under accelerations as $\frac{F_{PT}}{F_{FD}}$ varies from $\frac{0.10}{0.90}$ to $\frac{0.90}{0.10}$

5.1.2.2 Peak Rotation

The local responses of SC-EBF can be visualised in terms of peak link rotation (θ_{peak}) under various spectral accelerations ($S_a(T_1)$). From Figure 24, it is notable that θ_{peak} follows a similar pattern as IDR_{peak} and tends to increase in magnitude as the $\frac{F_{PT}}{F_{FD}}$ ratio increases. This aligns with the theory that energy dissipation in the link reduces as $\frac{F_{PT}}{F_{FD}}$ ratio increases, which magnify the rotation experienced by the SC-link.

One noticeable discrepancy between the results obtained from analyses and the expected results is the number of cases with θ_{peak} exceeding the threshold capacities. Referring to Lettieri et al.'s paper, the SC-link was designed to accommodate a design target rotation of 0.08 rad, which is the maximum permissible rotation of short link according to the Eurocode [2]. However, it is noticeable that large number of red and blue cases exceed the capacity of 0.08 rad. This suggests that further modifications should be made to the design of the SC-link to enhance its link rotation resistance.

Figure 25 displays the results of linear regression analyses of θ_{peak} , with red lines representing cases with uncertainties while the blue ones correspond to cases without uncertainties. The regression graphs reveal that the regression lines and 95% confidence intervals of both red cases (with uncertainties) and blue cases (without uncertainties) overlap with each other. This demonstrates that there is a high degree of agreement in θ_{peak} values between cases with and without uncertainties, indicating that uncertainty has a negligible impact on θ_{peak} in the SC-link.

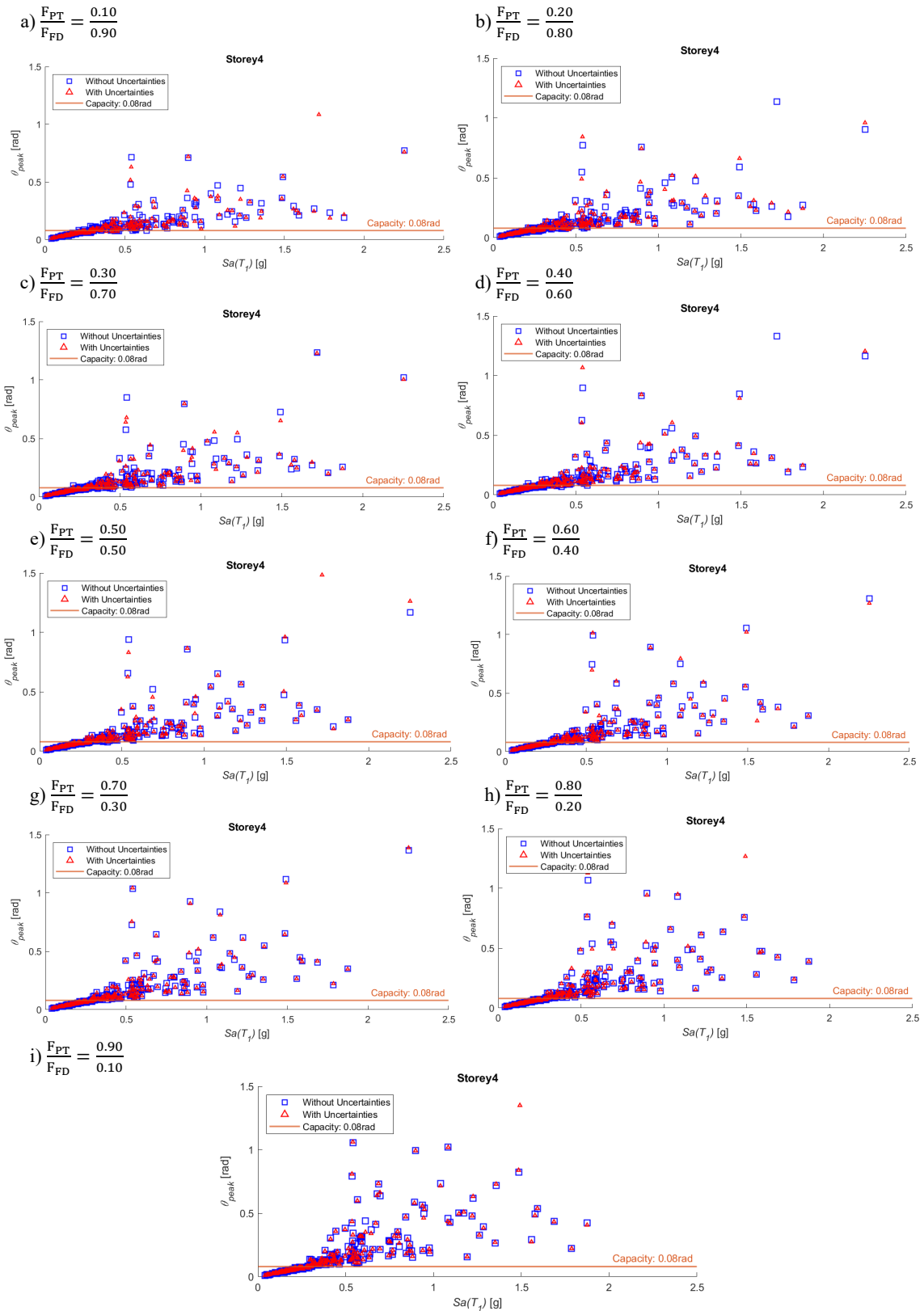


Figure 24 – Plots of peak link rotations (θ_{peak}) at storey 4 of SC-EBF under accelerations as

$$\frac{F_{PT}}{F_{FD}} \text{ varies from } \frac{0.10}{0.90} \text{ to } \frac{0.90}{0.10}$$

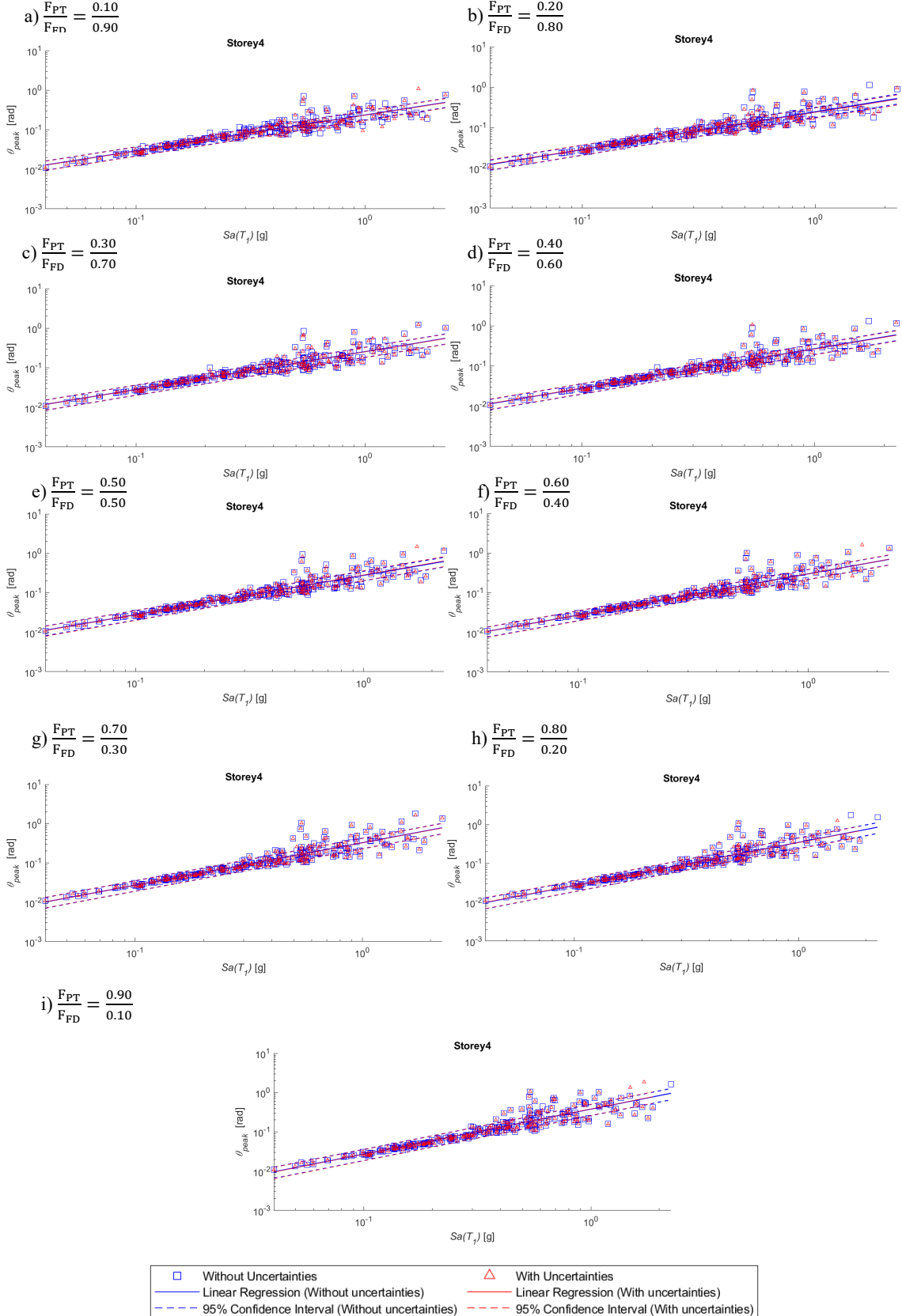


Figure 25 – Linear regression of peak link rotations (θ_{peak}) at storey 4 of SC-EBF under accelerations as $\frac{F_{PT}}{F_{FD}}$ varies from $\frac{0.10}{0.90}$ to $\frac{0.90}{0.10}$

5.1.2.3 Residual Interstorey Drift Ratio

Figure 26 displays nine logarithmic graphs that exhibit the relationship between residual interstorey drift ratios (IDR_{res}) and spectral acceleration ($S_a(T_1)$) at storey 4 of SC-EBF. The ratios of F_{PT} to F_{FD} ratios vary from $\frac{0.10}{0.90}$ to $\frac{0.90}{0.10}$. In each $\frac{F_{PT}}{F_{FD}}$ scenario, the data points in red represent 240 cases that take uncertainties into account while the 240 blue points are the cases where uncertainties are not considered. It can be observed that among all $\frac{F_{PT}}{F_{FD}}$ scenarios, IDR_{res} are very small at $S_a(T_1) < 0.1$ and jump to $IDR_{res} = 0.01\%$ at $S_a(T_1) > 0.1$. Upon comparison of the scenarios, it is evident that as $\frac{F_{PT}}{F_{FD}}$ increases, there is a consistent decrease in IDR_{res} , which is in line with the theory that the self-centring ability is enhanced by post-tensioning PT-bars with higher F_{PT} values. This phenomenon is particularly noticeable at the ranges of $\frac{0.4}{0.6}$ to $\frac{0.50}{0.50}$. The sudden decrease in large amount of IDR_{res} from $\frac{F_{PT}}{F_{FD}} = \frac{0.40}{0.60}$ to $\frac{F_{PT}}{F_{FD}} = \frac{0.50}{0.50}$ shows a good agreement with the theoretical behaviour of the SC-EBF previously explained by Lettieri et al. [5], indicating that the self-centring behaviour of the SC-EBF is only achieved when $F_{PT} \geq F_{FD}$, i.e. $\frac{F_{PT}}{F_{FD}} = \frac{0.50}{0.50}$, which makes the residual drifts tend to zero at this force ratio. It is also observed that at $\frac{F_{PT}}{F_{FD}} = \frac{0.50}{0.50}$, the cluster of larger IDR_{res} mainly occur in cases with uncertainties. This suggests that the presence of uncertainties affect the magnitude of IDR_{res} significantly only when $\frac{F_{PT}}{F_{FD}} = \frac{0.50}{0.50}$.

To further evaluate whether the presence of uncertainties will lead to exceedance of capacity for IDR_{res} , plots of IDR_{res} vs. $S_a(T_1)$ of SC-EBF storey 4 are presented in Figure 27. Two lines of capacity values, 0.2% for DS1 and 0.5% for DS2, are plotted to indicate the number of cases with IDR_{res} exceeding limiting values. The results show that while increasing $\frac{F_{PT}}{F_{FD}}$ generally reduces IDR_{res} on average, there are a few anomalous cases where IDR_{res} exceeds 0.2% and 0.5% between $\frac{F_{PT}}{F_{FD}} = \frac{0.30}{0.70}$ and $\frac{F_{PT}}{F_{FD}} = \frac{0.80}{0.20}$. This is attributed to the decrease in energy dissipation capacity as $\frac{F_{PT}}{F_{FD}}$ increases, which causes local deformations to occur within the frame and leads to residual drifts. The exceedance of capacity due to the presence of uncertainties is particularly obvious in scenario $\frac{F_{PT}}{F_{FD}} = \frac{0.40}{0.60}$, in which three cases with uncertainties exceed the threshold of DS1 (0.2%). However, these cases represent only 3 out of 480 cases, which can be considered negligible.

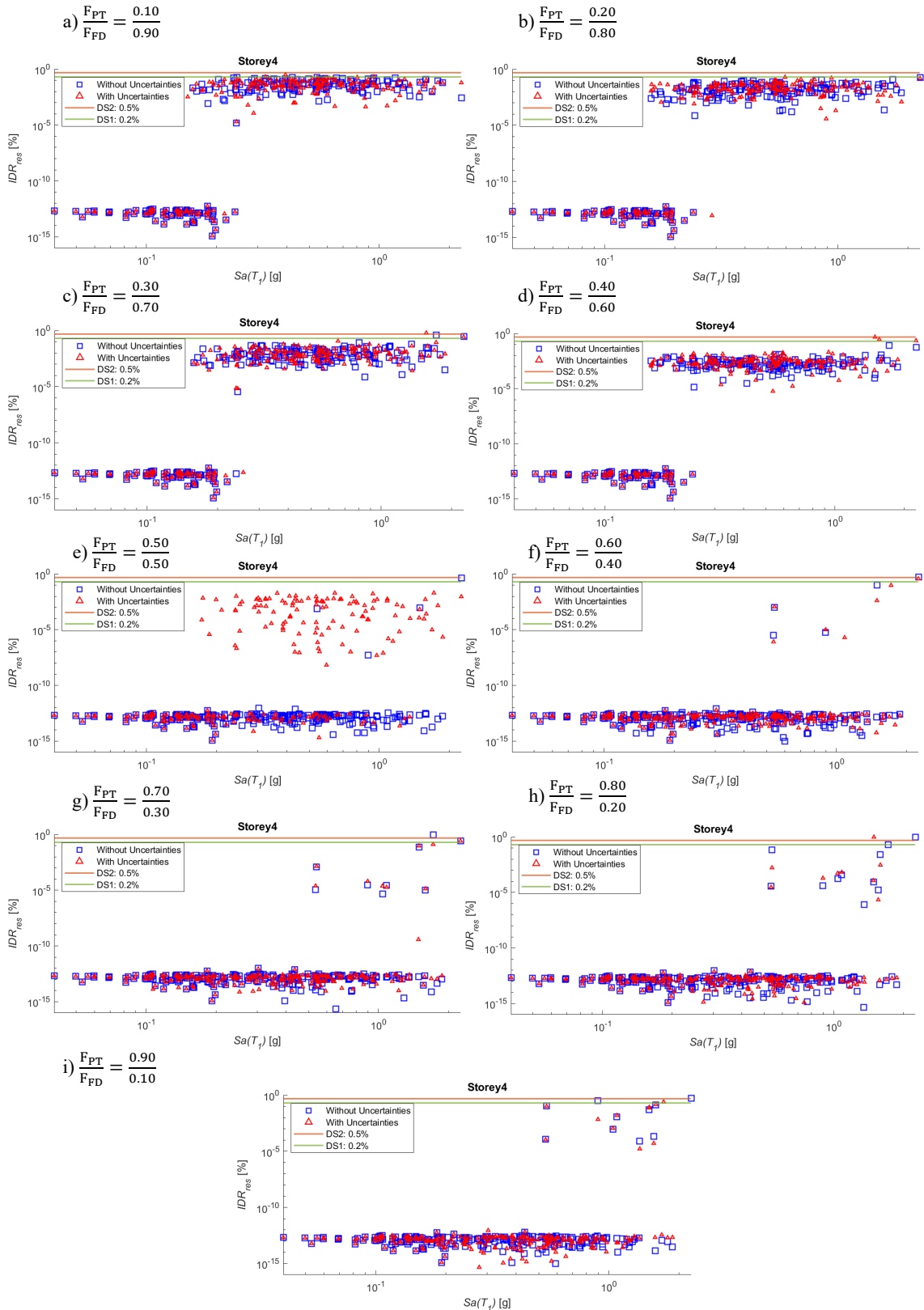


Figure 26 – Logarithmic plots of residual drift ratios at storey 4 of SC-EBF under accelerations as $\frac{F_{PT}}{F_{FD}}$

varies from $\frac{0.10}{0.90}$ to $\frac{0.90}{0.10}$

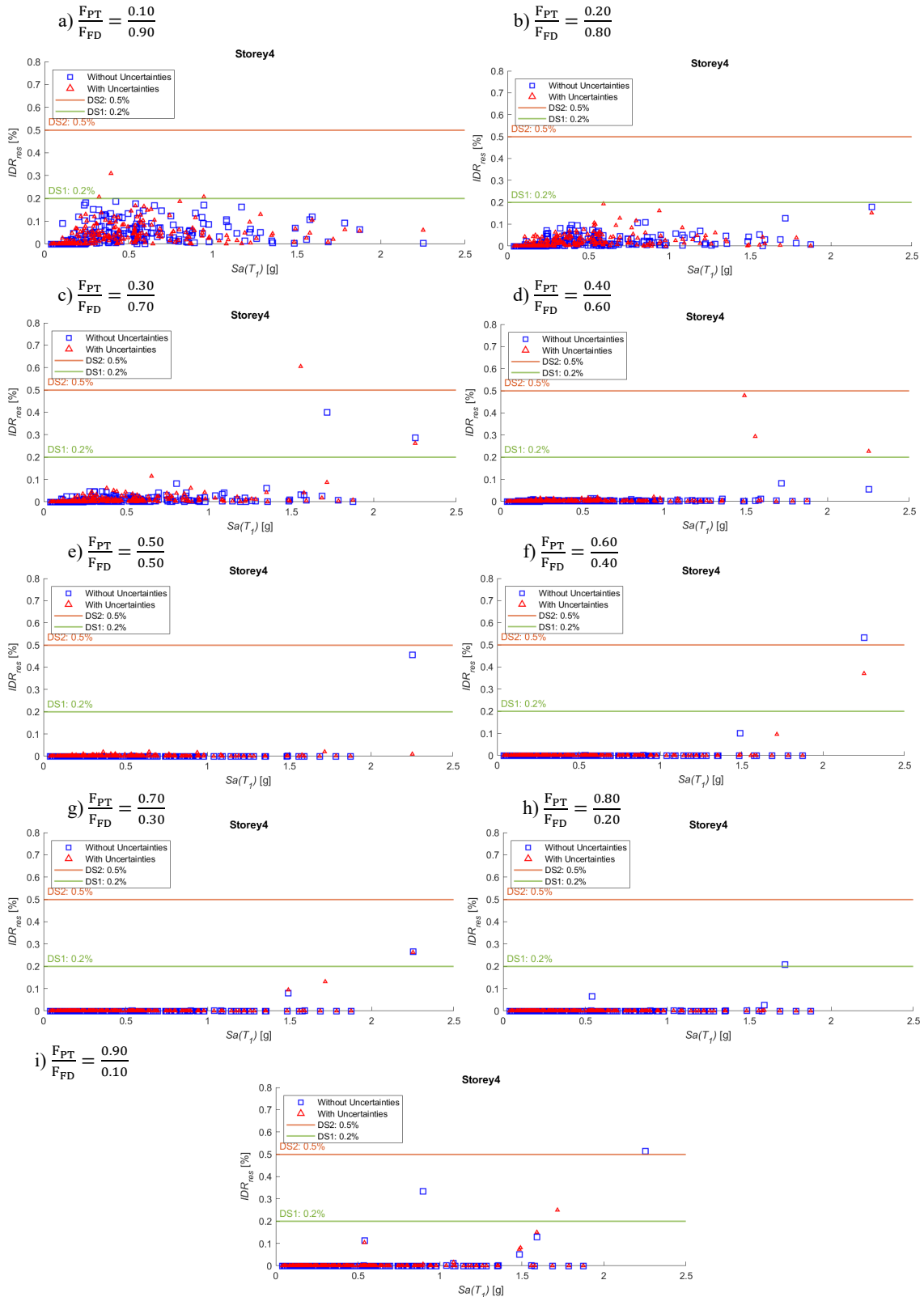


Figure 27 – Plots of residual drift ratios (IDR_{res}) at storey 4 of SC-EBF under accelerations as $\frac{F_{PT}}{F_{FD}}$ varies from $\frac{0.10}{0.90}$ to $\frac{0.90}{0.10}$

5.1.3 Fragility Curves of Residual Interstorey Drift Ratio

According to the previous section, it was found that there is only a negligible number of cases with IDR_{res} exceed the threshold of 0.2%. Thus, the fragility curves for IDR_{res} exceeding 0.2% cannot show the correlation between results considering uncertainties and those do not effectively. Hence, fragility curves for IDR_{res} are plotted for a lower value, at $IDR_{res} = 1 \times 10^{-10} \%$ to visualise the impact of uncertainties IDR_{res} values more effectively. This threshold was selected because when referring to the logarithmic graphs of IDR_{res} vs. $S_a(T_1)$ in Figure 26, it can be observed that the scatters are divided into two data clouds at $IDR_{res} = 1 \times 10^{-10} \%$. Hence, this value was considered a reliable reference for assessing the probability of occurrence of IDR_{res} .

Figure 28 displays the revised fragility curves indicating the probability of exceeding IDR_{res} of $1 \times 10^{-10} \%$ at storeys 4, as $\frac{F_{PT}}{F_{FD}}$ varies from $\frac{0.10}{0.90}$ to $\frac{0.90}{0.10}$. The curves in blue (without uncertainties) are nearly identical to the red curves (with uncertainties) for $\frac{F_{PT}}{F_{FD}}$ ratios between $\frac{0.10}{0.90}$ and $\frac{0.40}{0.60}$ and between $\frac{0.60}{0.40}$ and $\frac{0.90}{0.10}$, indicating that uncertainties have minimal impact on the probability of failure and the behaviour of the SC-EBF.

In contrast, at $\frac{F_{PT}}{F_{FD}} = \frac{0.50}{0.50}$, the probability of exceeding the threshold is considerably higher for the red cases, revealing that uncertainties have a significant effect on the seismic response of SC-EBF at a $\frac{F_{PT}}{F_{FD}}$ ratio of $\frac{0.50}{0.50}$. This finding is consistent with the logarithmic graphs of IDR_{res} vs. $S_a(T_1)$ in Figure 26, which demonstrates that the upper scatter cloud consists mainly of cases with uncertainties when $\frac{F_{PT}}{F_{FD}} = \frac{0.50}{0.50}$. This may be because as stated by Lettieri et al. [5], the self-centring behaviour in the SC-link is first achieved at $\frac{F_{PT}}{F_{FD}} = \frac{0.50}{0.50}$, which implies that its ability to prevent residual drifts is not as strong, thus increasing the impact of uncertainties on the seismic response.

Furthermore, it is visible that there is an increase in probability of failure $\frac{F_{PT}}{F_{FD}}$ increases with higher $\frac{F_{PT}}{F_{FD}}$ values. This agrees with the theory that self-centring behaviour is enhanced when more post-tensioning force, F_{PT} , is applied to the PT-bars in the SC-link.

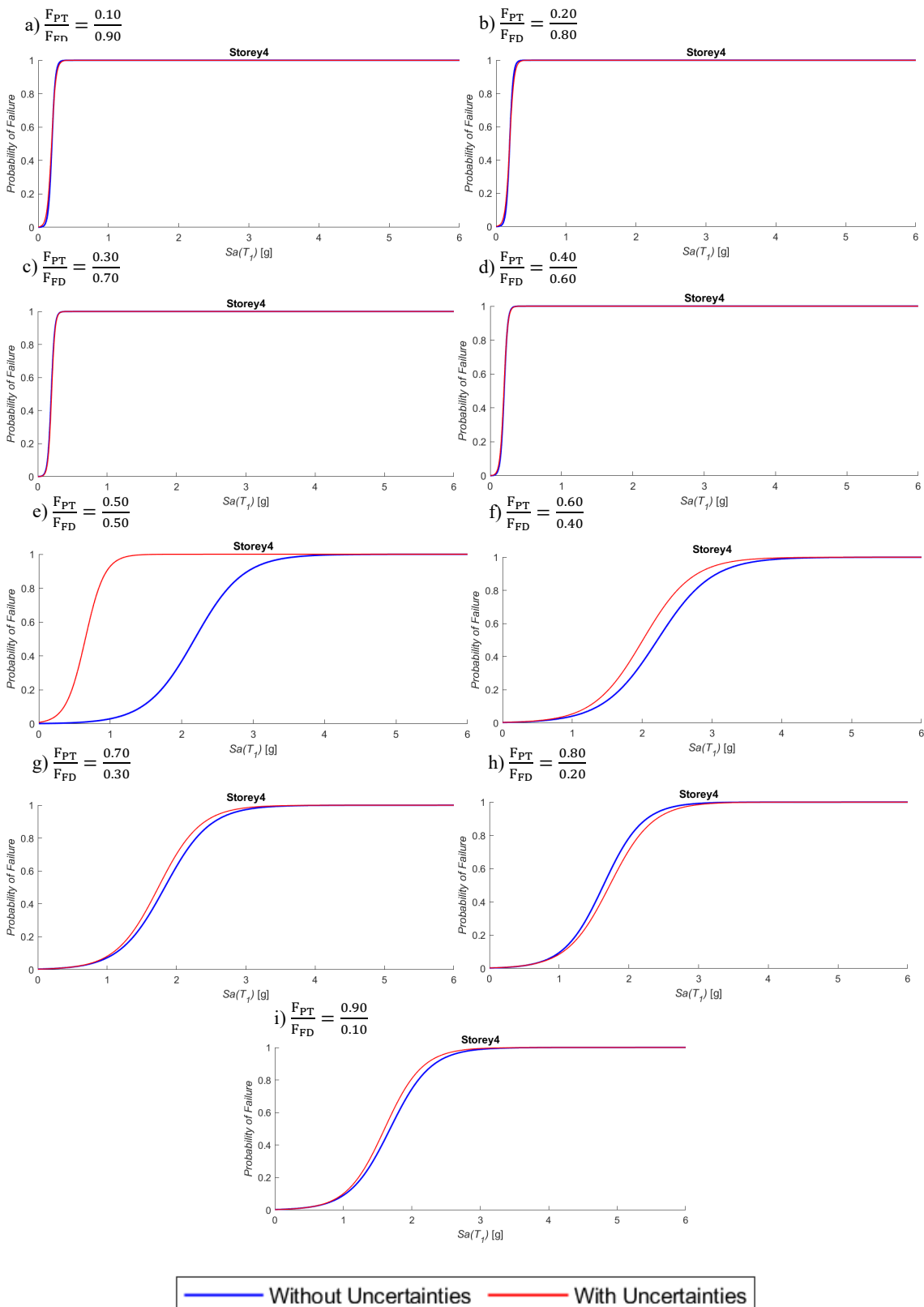


Figure 28 – Fragility curves for residual interstorey drift ratio (IDR_{res}) with a threshold of $DS1 = 1 \times 10^{-10}\%$ at storey 4 as $\frac{F_{PT}}{F_{FD}}$ varies from $\frac{0.10}{0.90}$ to $\frac{0.90}{0.10}$

5.2 Optimisation of SC-Link

To achieve the best balance between energy dissipation capacity and self-centring ability in the SC-link model, it is important to determine the optimal $\frac{F_{PT}}{F_{FD}}$ ratio. Figure 29, Figure 30 and Figure 31 illustrate the trends of IDR_{res} , IDR_{peak} and θ_{peak} under 30 scaled accelerograms at ultimate limit state ($S_a(T_1)_{ULS} = 1.2g$) as $\frac{F_{PT}}{F_{SC-link}}$, the ratio between F_{PT} and the total force in the SC-link ($F_{SC-link}$), is altered from 0.1 to 0.9. It should be noted that $\frac{F_{PT}}{F_{SC-link}} + \frac{F_{FD}}{F_{SC-link}} = 1$.

Figure 29 demonstrates that for both cases with uncertainties and without uncertainties, increasing F_{PT} leads to a general decrease in IDR_{res} . IDR_{res} generally tends to zero at $\frac{F_{PT}}{F_{SC-link}} = 0.5$ and then increase again at $\frac{F_{PT}}{F_{SC-link}} = 0.8$. Theoretically, increasing F_{PT} is expected to improve the self-centring behaviour of SC-EBF. However, when $\frac{F_{PT}}{F_{FD}} = \frac{0.80}{0.20}$ (i.e., $\frac{F_{PT}}{F_{SC-link}} = 0.80$), there is minimal energy dissipation in the SC-link due to the low value of F_{FD} in the friction device. As a consequence, an increase in local deformation will occur in the frame, which ultimately results in increased residual deformation. This can be proven by Figure 30 and Figure 31 which suggests that IDR_{peak} and θ_{peak} show a positive linear relationship with $\frac{F_{PT}}{F_{SC-link}}$, so as F_{PT} increases (i.e. F_{FD} decreases), IDR_{peak} and θ_{peak} increase accordingly. This supports the theory that reducing F_{FD} lowers energy dissipation, which in turn leads to higher peak deformations.

As previously mentioned, observations have shown that IDR_{res} starts to become zero at $\frac{F_{PT}}{F_{FD}} = \frac{0.50}{0.50}$. Therefore, $\frac{F_{PT}}{F_{FD}} = \frac{0.50}{0.50}$ is considered the ideal theoretical ratio. However, the fragility curve in Figure 28 reveals that uncertainties have the greatest impact on SC-EBF when $\frac{F_{PT}}{F_{FD}} = \frac{0.50}{0.50}$, making it an unfavourable ratio. Moreover, energy dissipation capacity increases as $\frac{F_{PT}}{F_{FD}}$ decreases. Therefore, to achieve both self-centring ability and maximum energy dissipation, the optimal $\frac{F_{PT}}{F_{FD}}$ should be between $\frac{0.50}{0.50}$ and $\frac{0.60}{0.60}$, and F_{FD} should be maximised to enhance energy dissipation while avoiding residual deformation, even in the presence of uncertainty.

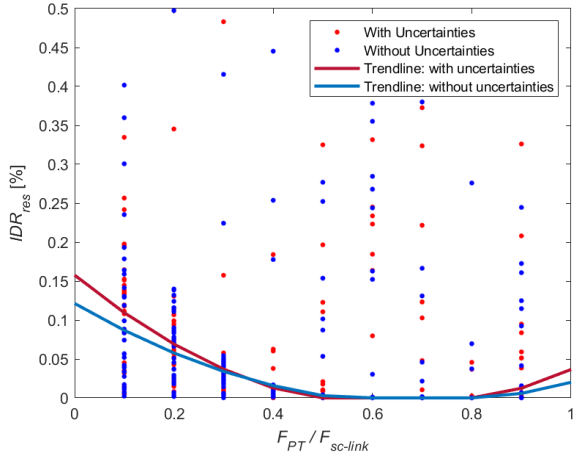


Figure 29 – General trends of residual interstorey drift ratio (IDR_{res}) as $\frac{F_{PT}}{F_{FD}}$ varies from $\frac{0.10}{0.90}$ to $\frac{0.90}{0.10}$

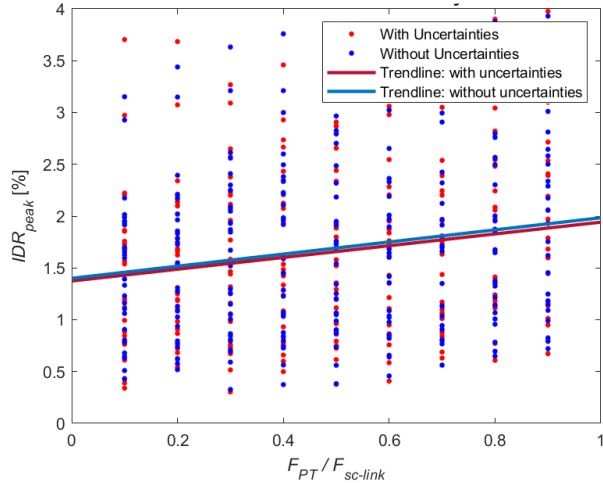


Figure 30 – General trends of peak interstorey drift ratio (IDR_{peak}) as $\frac{F_{PT}}{F_{FD}}$ varies from $\frac{0.10}{0.90}$ to $\frac{0.90}{0.10}$

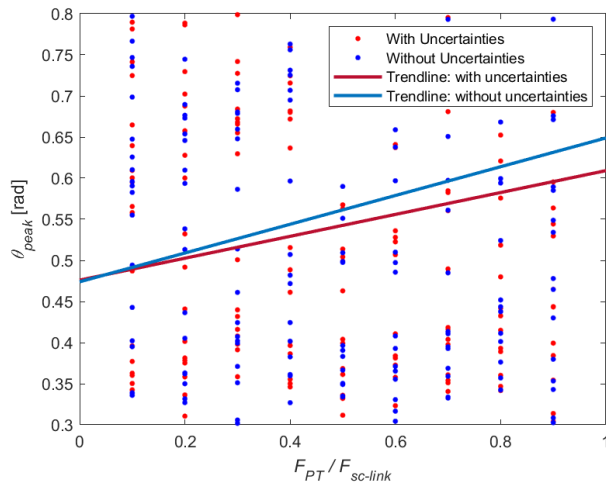
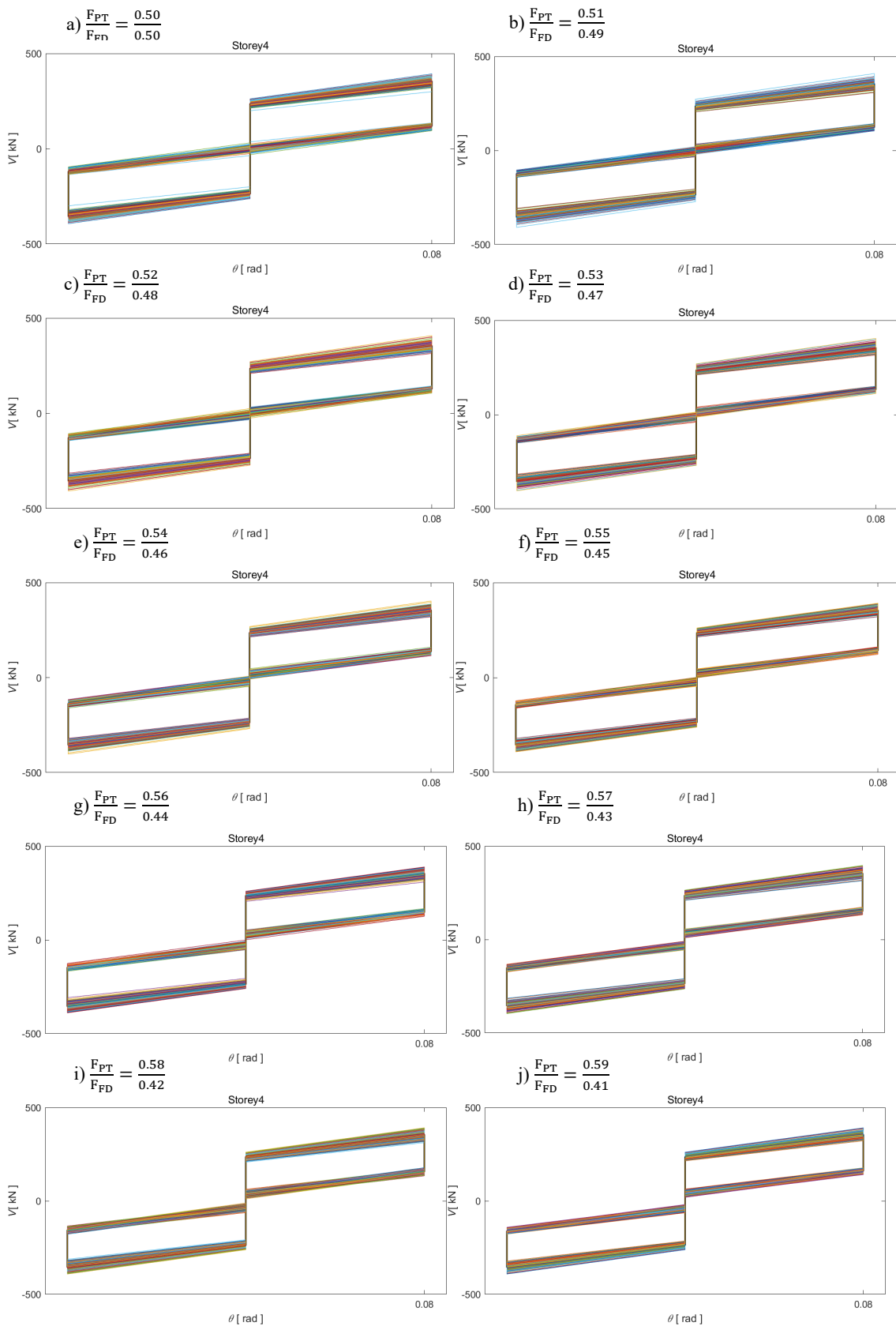


Figure 31 – General trends of peak link rotation (θ_{peak}) as $\frac{F_{PT}}{F_{FD}}$ varies from $\frac{0.10}{0.90}$ to $\frac{0.90}{0.10}$

Since residual deformation corresponds to the deformation in the frame after it is unloaded, residual deformation can be detected as the maximum deformation at zero shear force in the hysteretic loops of SC-links in terms of transverse shear force vs. link. Figure 32 displays the hysteretic behaviour of SC-links with $\frac{F_{PT}}{F_{FD}}$ ratios ranging from $\frac{0.50}{0.50}$ to $\frac{0.60}{0.40}$. Each graph in Figure 32 overlays the hysteretic loops of 240 cases that consider uncertainties, along with the design case that do not consider uncertainties. By comparing the hysteretic loops of different $\frac{F_{PT}}{F_{FD}}$ ratios, when $\frac{F_{PT}}{F_{FD}}$ ratio is within the range of $\frac{0.50}{0.50}$ to $\frac{0.55}{0.45}$, the link rotations are not all zero when no shear force is presented. Thus, it is evident that residual link rotations occur due to uncertainties. Notably, as can be observed in Figure 32(g), when $\frac{F_{PT}}{F_{FD}} = \frac{0.56}{0.44}$, there is no link rotation at $V = 0$, signifying that $\frac{F_{PT}}{F_{FD}} = \frac{0.56}{0.44}$ is the minimum ratio that exhibits no residual rotation, making it the optimal ratio to provide the SC-link with self-centring ability and maximum energy dissipation capacity.



$$k) \frac{F_{PT}}{F_{FD}} = \frac{0.60}{0.40}$$

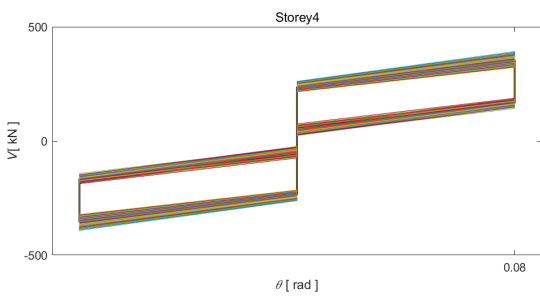


Figure 32 – Hysteretic behaviour in terms of transverse shear force (V) vs. link rotation (θ) as $\frac{F_{PT}}{F_{FD}}$ varies
from $\frac{0.50}{0.50}$ to $\frac{0.60}{0.40}$

6 CONCLUSION

This paper presents a performance assessment of a damage free self-centring link (SC-link) for eccentrically braced frames (EBFs) proposed by Lettieri et al. [5]. It aims to provide insight into effect of uncertainties in the SC-link model on the SC-EBF and suggests an optimisation approach for the SC-link model.

A four-storey, one bay SC-EBF was taken from a steel residential building with a four-storey, five-bays by three-bays configuration as a case study. The structure was modelled in Opensees as a 2D nonlinear finite element model. It was identified from literature that uncertainties in the SC-link primarily arise from the dynamic friction coefficient (μ) of the friction device (FD), the post-tensioning force ($F_{p,PT}$) in each of the post-tensioned bars (PT-bars) and the prestressed force ($F_{p,FD}$) in each of the bolts of the friction device. The median values and coefficient of variations of μ , $F_{p,PT}$ and $F_{p,FD}$ were obtained from literature and their distributions were identified. Various sets of values were selected from the distributions to model and analyse different SC-link models to account for model uncertainties. A set of 240 ground motion records were used to conduct modal analysis and non-linear dynamic analysis accounting for record-to-record uncertainties. It was also discovered that the ratio of total post-tensioning force in the PT-bars to the total friction force in FDs ($\frac{F_{PT}}{F_{FD}}$ ratio) affect the behaviour of the SC-link model. Thus, analyses were performed on SC-links with different $\frac{F_{PT}}{F_{FD}}$ ratios to find the ratio that experience greatest impact from uncertainties and the optimal ratio for the SC-link model. Peak interstorey drift ratio (IDR_{peak}), peak link rotation (θ_{peak}) and residual interstorey drift ratio (IDR_{res}) were chosen as engineering demand parameters and spectral acceleration of the fundamental period ($S_a(T_1)$) was chosen as the intensity measure. The results of the SC-link analyses considering uncertainties were compared with those without uncertainties. Linear regression analyses were conducted on IDR_{peak} and θ_{peak} , while fragility analyses were performed on IDR_{res} to aid the comparison of models with and without uncertainties. Furthermore, an additional set of 30 ground motion records were scaled at ultimate limit state to analyse SC-link models and determine how IDR_{peak} , θ_{peak} and IDR_{res} vary with $\frac{F_{PT}}{F_{FD}}$ ratios to identify the optimal ratio.

Some main findings were identified from this study and described in the following: (1) comparison of hysteretic behaviours of cases with and without uncertainties shows that uncertainties cause variation in hysteretic responses, leading to increased risk of residual deformation; (2) comparison of the regression analyses on IDR_{peak} and θ_{peak} of cases with and

without uncertainties indicates that all cases display nearly identical regression and dispersion lines, suggesting that uncertainties have negligible impact on values of IDR_{peak} and θ_{peak} . However, small number cases exceed the threshold values due to the presence of uncertainties when IDR_{peak} against their capacities. Nonetheless, this is still considered as negligible due to the low probability of exceedance; (3) results of θ_{peak} reveals that a large number of cases exceed the maximum permissible link rotation suggested by the Eurocode [2], indicating that further modifications should be made in enhancing the rotation resistance of the link; (4) comparing the fragility analyses result on IDR_{res} of cases with and without uncertainties reveals that uncertainties have nearly no impact on IDR_{res} between $\frac{F_{PT}}{F_{FD}} = \frac{0.10}{0.90}$ and $\frac{F_{PT}}{F_{FD}} = \frac{0.40}{0.60}$, most significant impact on IDR_{res} as $\frac{F_{PT}}{F_{FD}} = \frac{0.50}{0.50}$ and small impact between $\frac{F_{PT}}{F_{FD}} = \frac{0.60}{0.40}$ and $\frac{F_{PT}}{F_{FD}} = \frac{0.90}{0.10}$. This suggests that $\frac{F_{PT}}{F_{FD}} = \frac{0.50}{0.50}$ is an unfavourable ratio for the SC-link model; (5) a good agreement is observed between the trend of IDR_{peak} , θ_{peak} and IDR_{res} obtained from analyses and predicted from theory; (6) the trends indicate that the optimal ratio lies between $\frac{F_{PT}}{F_{FD}} = \frac{0.50}{0.50}$ and $\frac{F_{PT}}{F_{FD}} = \frac{0.60}{0.40}$ and it was ultimately found that the optimal ratio is $\frac{0.56}{0.44}$.

7 FUTURE WORK

The following suggestions for improvements and future work are proposed:

1. Referring to the resulting peak link rotations obtained from the cloud analysis, it was observed that a large number of cases exceed the designed maximum link rotations. Thus, modifications are suggested to be made to enhance the rotation resistance of the SC-link model.
2. In this study, only the model uncertainties arise from the post-tensioning force in the PT-bars, prestressed forced in the bolts of the friction devices, and the friction coefficient of the friction device were considered. However, the SC-link comprises different structural elements with varying material properties and sizes, which could lead to additional uncertainties. Therefore, future research could explore more sources of uncertainty to provide a comprehensive assessment of model uncertainties in the SC-link.
3. During the cloud analyses, only 240 spectral accelerations ($S_a(T_1)$) ranging from 0 to 2.5g were taken into account. However, when fragility analyses were conducted on the residual interstorey drift ratio, the fragility curves were plotted up to a $S_a(T_1)$ of 6g to achieve a probability of 1 in the graph. Consequently, if there were no occurrences of exceeding DS1 at $S_a(T_1)$ values between 0 and 2g, it would be impractical to estimate the probability of failure at higher $S_a(T_1)$ values. Therefore, to obtain a more accurate fragility estimation, future analyses could include more accelerations from the range of 2.5g to 6g.
4. In this paper, the hysteretic behaviours of the SC-link were explored by utilising the analytical equations proposed by Lettieri et al. [5]. However, the global hysteretic behaviour of the frame was not investigated. To provide a more comprehensive assessment of the SC-EBF, future research can employ push-pull analyses in OpenSees to as well capture the hysteretic behaviour of the SC-EBF.

8 Reference

1. World Economic Forum. A Vision for Managing Natural Disaster Risk Proposals for Public/Private Stakeholder Solutions. 2011.
2. British Standards Institution. Eurocode 8: Design of Structures for Earthquake Resistance-Part 1: General rules, Seismic Actions and Rules for Buildings. 1998.
3. Gledhill S. Steel Moment Frames with Sliding Hinge Joints-Lessons Learnt during Implementation [Internet]. 2013. Available from: <https://www.researchgate.net/publication/280858419>
4. Pampanin S. Reality-check and Renewed Challenges in Earthquake Engineering: Implementing Low-damage Structural Systems-from Theory to Practice. 2012.
5. Lettieri A, de la Peña A, Freddi F, Latour M. Damage-free self-centring links for eccentrically braced frames: development and numerical study. *J Constr Steel Res.* 2023 Feb 1;201.
6. Macrae GA, Charles Clifton G, Mackinven H, Mago N, Butterworth J, Pampanin S. The Sliding Hinge Joint Moment Connection. 2010.
7. Hjelmstad KD, Popov EP, Asce F. Characteristics of Eccentrically Braced Frames. 1984.
8. Macrae G, Clifton C. Low Damage Design of Steel Structures Organized by Steel Construction New Zealand. 2013.
9. Moderini LK. Impact of Model Uncertainties on the Seismic Response of Eccentrically Braced Steel Frames with Self-Centring Links. 2022.
10. Popov EP, Engelhardt MD. Seismic Eccentrically Braced Frames. Vol. 10, *J. Construct. Steel Research.* 1988.
11. Stratan A. Bolted Links for Eccentrically Braced Steel Frames. In 2004.
12. Ioan A, Stratan A, Dubină D, Poljanšek M, Molina FJ, Taucer F, et al. Experimental validation of re-centring capability of eccentrically braced frames with removable links. *Eng Struct.* 2016 Apr 15;113:335–46.
13. Dubina D, Stratan A, Dinu F. Dual High-strength Steel Eccentrically Braced Frames with Removable Links. *Earthq Eng Struct Dyn.* 2008;37(15):1703–20.
14. Mansour N, Christopoulos C, Tremblay R. Experimental Validation of Replaceable Shear Links for Eccentrically Braced Steel Frames. *Journal of Structural Engineering.* 2011 Oct;137(10):1141–52.
15. Bozkurt MB, Topkaya C. Replaceable Links with Direct Brace Attachments for Eccentrically Braced Frames. *Earthq Eng Struct Dyn.* 2017 Oct 25;46(13):2121–39.
16. Zhong C, Christopoulos C. Self-centering Seismic-resistant Structures: Historical Overview and State-of-the-art. *Earthquake Spectra.* 2022 May 1;38(2):1321–56.
17. Chancellor NB, Eatherton MR, Roke DA, Akbas T. Self-centering Seismic Lateral Force Resisting Systems: High Performance Structures for the City of Tomorrow. Vol. 4, *Buildings.* MDPI AG; 2014. p. 520–48.
18. Cheng CT, Hsu H, Lin KC. Seismic Behavior of Self-centering Designed Eccentrically Braced Frames. 2012.
19. Tong L, Zhang Y, Zhou X, Keivan A, Li R. Experimental and Analytical Investigation of D-Type Self-Centering Steel Eccentrically Braced Frames with Replaceable Hysteretic Damping Devices. *Journal of Structural Engineering.* 2019 Jan;145(1).
20. Keivan A, Zhang Y. Seismic Performance Evaluation of Self-centering K-type and D-type Eccentrically Braced Frame Systems. *Eng Struct.* 2019 Apr 1;184:301–17.
21. Xu X, Zhang Y, Luo Y. Self-centering eccentrically braced frames using shape memory alloy bolts and post-tensioned tendons. *J Constr Steel Res.* 2016 Oct 1;125:190–204.

-
22. Xu X, Zhang Y, Luo Y. Self-centering Modularized Link Beams with Post-tensioned Shape Memory Alloy Rods. *Eng Struct.* 2016 Apr 1;112:47–59.
23. Buljak V, Ranzi G. Shape Memory Alloys. In: Constitutive Modeling of Engineering Materials [Internet]. Elsevier; 2021. p. 293–313. Available from: <https://linkinghub.elsevier.com/retrieve/pii/B9780128146965000149>
24. Garmeh V, Akbarpour A, Adibramezani M, Hojat Kashani A, Adibi M. SMA-based Self-centering Eccentrically Braced Frame with Vertical Link Member. *Structures.* 2022 Sep 1;43:1230–58.
25. Tubaldi E, Barbato M, Dall'Asta A. Influence of Model Parameter Uncertainty on Seismic Transverse Response and Vulnerability of Steel-Concrete Composite Bridges with Dual Load Path. *Journal of Structural Engineering.* 2012 Mar;138(3):363–74.
26. The Regents of the University of California. Open System for Earthquake Engineering Simulation - Home Page [Internet]. 2006 [cited 2022 Nov 28]. Available from: <https://opensees.berkeley.edu/>
27. Reinhorn AM, Willford MR. Nonlinear Structural Analysis For Seismic Design A Guide for Practicing Engineers Gregory G. Deierlein [Internet]. 2010. Available from: www.curee.org
28. Jeff Erochko. SelfCentering Material: Flag-Shaped Hysteresis with Slip Deformation and Bearing [Internet]. [cited 2023 Mar 19]. Available from: <https://opensees.berkeley.edu/OpenSees/manuals/usermanual/4160.htm>
29. British Standards Institution. Execution of Steel Structures and Aluminium Structures. Part 2: Technical Requirements for Steel Structures. BSI; 2011. 209 p.
30. Cavallaro GF, Francavilla AB, Latour M, Piluso V, Rizzano G. Cyclic Response of Low Yielding Connections Using Different Friction Materials. *Soil Dynamics and Earthquake Engineering.* 2018 Nov 1;114:404–23.
31. Jayaram N. New Ground Motion Selection Procedures and Selected Motions for the Peer Transportation Research Program. 2011.
32. Kroese DP. Monte Carlo Methods [Internet]. 2011. Available from: <http://www.maths.uq.edu.au/>
33. Fu ZF, He J. Modal Analysis - 1st Edition. Elseivier. Butterworth Heinemann; 2001. 304 p.
34. COMSOL. Rayleigh Damping [Internet]. 2023. [cited 2023 Apr 7]. Available from: https://doc.comsol.com/5.5/doc/com.comsol.help.sme/sme_ug_modeling.05.083.html
35. Guillermo Giraldo. Computing Rayleigh Damping Coefficients | Knowledge Base | SimScale [Internet]. 2021 [cited 2023 Apr 7]. Available from: <https://www.simscale.com/knowledge-base/rayleigh-damping-coefficients/>
36. Whittaker A. Engineering demand parameters for structural framing systems NHERI SimCenter View project Dynamic Topology Optimization of Rocking Spine Systems View project. 2004; Available from: <https://www.researchgate.net/publication/242693717>
37. Iwata Y, Sugimoto H, Kuwamura H. Reparability Limit of Steel Structural Buildings Based on the Actual Data of the Hyogoken-Nanbu Earthquake. 2002.
38. McCormick J, Aburano H, Nakashima M. Permissible Residual Deformation Levels for Building Structures Considering Both Safety and Human Elements. 2008.
39. Applied Technology Council. FEMA P58-1, Seismic Performance Assessment of Buildings, in: Volume 1-Methodology [Internet]. 2012. Available from: www.ATCouncil.org
40. Vamvatsikos D, Allin Cornell C. Incremental dynamic analysis. *Earthq Eng Struct Dyn.* 2002;31(3):491–514.

-
41. Gangolu J, Kumar A, Bhuyan K, Sharma H. Probabilistic demand models and performance-based fragility estimates for concrete protective structures subjected to missile impact. Reliab Eng Syst Saf. 2022 Jul 1;223.
 42. Belyadi H, Haghigat A. Supervised learning. Machine Learning Guide for Oil and Gas Using Python. 2021 Jan 1;169–295.
 43. Ambrosius WT. Topics in Biostatistics. 2007.